Climate Dynamics manuscript No.
(will be inserted by the editor)

Contribution of Tropical Instability Waves to ENSO Irregularity

Ryan M. Holmes · Shayne McGregor · Agus Santoso · Matthew H. England

Received: date / Accepted: date

Abstract Tropical instability waves (TIWs) are a major source of internally-generated oceanic variability in the equatorial Pacific Ocean. These non-linear phenomena play an important role in the sea surface temperature (SST) budget in a region critical for low-frequency modes of variability such as the El Niño-Southern Oscillation (ENSO). However, the direct contribution of TIW-driven stochastic variability to ENSO has received little attention. Here, we investigate the influence of TIWs on ENSO using a 1/4° ocean model coupled to a simple atmosphere. The use of a simple atmosphere removes complex

R. M. Holmes
Climate Change Research Centre, ARC Centre of Excellence for Climate System Science and the School of Mathematics and Statistics, University of New South Wales, Sydney, Australia
E-mail: ryan.holmes@unsw.edu.au

S. McGregor
School of Earth, Atmosphere and Environment, Monash University, Melbourne, Australia.

A. Santoso
Climate Change Research Centre and ARC Centre of Excellence for Climate System Science, University of New South Wales, Sydney, Australia. The Centre for Southern Hemisphere Oceans Research (CSHOR), CSIRO, Hobart, Australia.

M. H. England
Climate Change Research Centre and ARC Centre of Excellence for Climate System Science, University of New South Wales, Sydney, Australia.

intrinsic atmospheric variability while allowing the dominant mode of air-sea coupling to be represented as a statistical relationship between SST and wind stress anomalies. Using this hybrid coupled model, we perform a suite of coupled ensemble forecast experiments initiated with wind bursts in the western Pacific, where individual ensemble members differ only due to internal oceanic variability. We find that TIWs can induce a spread in the forecast amplitude of the Niño 3 SST anomaly six-months after a given sequence of WWBs of approximately $\pm 45\%$ the size of the ensemble mean anomaly. Further, when various estimates of stochastic atmospheric forcing are added, oceanic internal variability is found to contribute between about 20% and 70% of the ensemble forecast spread, with the remainder attributable to the atmospheric variability. While the oceanic contribution to ENSO stochastic forcing requires further quantification beyond the idealized approach used here, our results nevertheless suggest that TIWs may impact ENSO irregularity and predictability. This has implications for ENSO representation in low-resolution coupled models.

Keywords Tropical Instability Waves · El Niño - Southern Oscillation · Ocean General Circulation Model · Hybrid Coupled Model · Stochastic Forcing · Predictability

1 Introduction

Tropical Instability Waves (TIWs) are the dominant form of eddy variability in the tropical Pacific Ocean. They have timescales of 15-40 days, wavelengths of 700-1600km and their intensity varies seasonally and interannually with the strength of the equatorial circulation (Dueing et al, 1975; Legeckis, 1977; Contreras, 2002; Willett et al, 2006; Lyman et al, 2007; An, 2008). TIWs play an important role in the heat and momentum budget of the large-scale flow and influence the SST (Menkes et al, 2006; Jochum and Murtugudde, 2006). Through their SST anomalies TIWs directly alter the atmospheric surface winds at TIW scales (Chelton et al, 2001; Narapusetty and Kirtman, 2014), an effect that is known to feedback onto the TIWs themselves and influence the oceanic and atmospheric mean states (Pezzi et al, 2004; Zhang, 2014). While the dynamics of TIWs and their impacts on the mean equatorial circulation are well understood, their influence on interannual variability in the tropics has received less attention, beyond a number of studies on the contribution of TIW lateral heat fluxes to ENSO asymmetry (e.g. An, 2009; Imada and Kimoto, 2012), and rectification of TIW-associated small-scale atmospheric variability (Zhang and Busalacchi, 2008; Zhang, 2016). This is a particularly pertinent point given that TIWs are not fully resolved in the typical 1° ocean models used to study ENSO (Graham, 2014)[1], and that many coupled models underestimate SST variability in the eastern Pacific where TIWs are most active (Latif et al, 2001).

TIWs gain energy from non-linear hydrodynamic instabilities (Philander, 1976; Cox, 1980; Masina et al, 1999; Holmes and Thomas, 2016) that have a stochastic element. Therefore, the phasing and strength of TIWs can vary randomly, independent of variations in the mean circulation from which the TIWs gain energy. This internal stochastic oceanic variability is thought to contribute to interannual variability in ocean-only (Jochum and Murtugudde, 2004, 2005; von Schuckmann et al, 2008) and SST-forced atmosphere-only (Jochum et al, 2007b) models and can influence the skill of seasonal forecasts (Ham and Kang, 2011). Jochum et al (2007b) found that including TIW SST variability in the forcing of an atmospheric model increased wind and rainfall variability near the equator and near ±25° latitude by up to 35%. Jochum and Murtugudde (2004) and Jochum et al (2007b) suggest that the SST and wind stress variability induced by TIWs in the eastern Pacific is comparable to that driven by the Madden-Julian Oscillation (MJO) in the western Pacific, and thus could potentially contribute to the irregularity of the ENSO cycle. However, this hypothesis has not yet been investigated in depth in the literature.

[1] A form of TIWs can exist in these low-resolution models, and a correct representation of them within 1° models may be possible with an appropriate choice of viscosity (Jochum et al, 2008).

Stochastic forcing of the ENSO cycle is thought to stem mainly from internal atmospheric variability, in particular from wind bursts in the western Pacific associated with tropical cyclones and MJO events (Keen, 1982; Zhang, 2005). Such wind bursts can stochastically generate SST anomalies in the central and eastern Pacific via the zonal advection and thermocline depth anomalies associated with equatorial Kelvin waves, contributing to the irregularity of the ENSO cycle (Moore and Kleeman, 1999; Zavala-Garay et al, 2003). The strength and frequency of western Pacific wind bursts is thought to be dependent on the ENSO state, contributing to the asymmetry and diversity of ENSO events (Eisenman et al, 2005; Gebbie et al, 2007; Levine et al, 2016; Levine and Jin, 2017; Hayashi and Watanabe, 2017). The response of the ocean to a given wind burst is also thought to depend on the oceanic background state (Hu et al, 2014; Puy et al, 2016). However, in the eastern Pacific Puy et al (2016) found that this dependence was less clear due to TIW-driven noise and its rectification onto the mean state. This suggests that oceanic-sourced noise may also contribute to ENSO variability, in addition to noise sourced in the atmosphere. Finally, Holmes and Thomas (2016) found that TIWs act to damp the heat anomalies induced by intraseasonal Kelvin waves, which may impact the ability of Kelvin waves to kick-start the air-sea feedbacks necessary to initiate ENSO events.

In this study, we investigate how internal oceanic variability associated with TIWs influences the growth and amplitude of ENSO events. We use a $1/4^{\circ}$ resolution Pacific basin-wide ocean model coupled to a simplified atmospheric model and focus on the strong TIW and ENSO growth season of July-December. The simple atmospheric model is designed to isolate the effect of TIW-driven noise on coupled variability, as internal atmospheric variability associated with a fully-dynamic atmosphere is absent. Hybrid coupled models that utilize a simplified atmosphere, ocean, or both, have been used extensively in the study of ENSO predictability, irregularity, frequency, seasonality, asymmetry and the role of stochastic forcing (e.g. Neelin, 1990; Kirtman, 1997; Blanke et al, 1997; Zavala-Garay et al, 2003). However, there are several key differences between these models used in the past and our model. Firstly, our higher resolution 1/4° ocean model better resolves TIWs and their significant contribution to the upper-ocean heat budget (Menkes et al, 2006), which is likely underestimated in lower resolution models (Graham, 2014). Secondly, we use an atmospheric boundary layer model (ABLM) in the atmosphere (Seager et al, 1995; Deremble et al, 2013). Both these elements facilitate a focus on the role of complex non-linear ocean dynamics in ENSO, and also provide a comparison with previous hybrid models that have utilized full atmospheric GCMs coupled to simple ocean models (e.g. Dommenget, 2010; Frauen and Dommenget, 2010).

The article is organized as follows. In Section 2 we describe the modeling setup; the ocean model, the various atmospheric forcing data sets and the simplified atmospheric model. In Section 3 we examine the influence of the oceanic internal variability on SST variability without the statistical atmospheric coupling (i.e. an uncoupled system with constant wind stress forcing). In Section 4 we then examine the influence of this variability within an ensemble of coupled forecast experiments. Section 5 compares the impact of oceanic internal variability with several different estimates of stochastic atmospheric forcing. The results are discussed and summarized in Section 6.

2 Model and Experimental Design

2.1 The Ocean Model

We use the Regional Ocean Modeling System (ROMS, Shchepetkin and McWilliams, 2005) ocean model in a configuration, adapted from Holmes and Thomas (2016), that spans the tropical Pacific Ocean (105°E to 70°W, 30°S to 30°N) with 0.25° horizontal resolution, 50 vertical levels and a time step of 10 minutes. At the western and meridional boundaries temperature and salinity are nudged to climatological values from the World Ocean Atlas 2013 (WOA13, Locarnini et al, 2013; Zweng et al, 2013) and the horizontal velocity is nudged to zero. The K-profile parameterization is used to parameterize sub-grid scale vertical mixing processes (Large et al, 1994). We use a diurnal cycle in shortwave radiation as we found this to be necessary to correctly represent the shear and stratification in the upper Equatorial Undercurrent (EUC). Horizontal diffusion of momentum was achieved with a bi-harmonic viscosity with coefficient $1 \times 10^{11} \mathrm{m}^4\mathrm{s}^{-1}$, and harmonic horizontal diffusion of temperature and salinity was included with coefficient $100\mathrm{m}^2\mathrm{s}^{-1}$. ROMS has been successfully used for process studies of TIWs under similar configurations (Marchesiello et al, 2011; Holmes and Thomas, 2016).

2.2 The Control Atmospheric Forcing

To simplify the analysis and interpretation, we use a temporally-constant control atmospheric forcing set. This idealization allows the role of internal oceanic variability associated with TIWs to be cleanly isolated from atmospheric variability. Surface forcing fields are taken from a July-December average of the ERA-Interim 1980-2014 data set (Dee et al, 2011). This season has strong trade winds, with energetic TIWs (Contreras, 2002), and is the typical growth period for ENSO events which peak in December-January-February (Tziperman et al, 1997), thus ideal for this process study.

Using a temporal average of the ERA-Interim atmospheric state variables (e.g. six monthly-averaged wind speed) can cause inaccuracies in the heat flux and wind stress derived from these variables as quadratic terms in the bulk formula, involving temporal correlations between variables, are ignored (e.g. see Penduff et al, 2011). To avoid this problem here we use the ERA-Interim data to explicitly prescribe both the wind stress, capturing the non-linearities in the momentum forcing, and the wind speed magnitude (as opposed to its two components), thereby retaining the correct wind speed magnitude in the bulk calculation of the latent and sensible heat fluxes. This does not correct for all the quadratic correlation terms in the bulk formula, but the remaining biases are acceptable for the idealized nature of the experiments performed here, as will be discussed shortly.

A simulation using the ERA-Interim forcing described above was spun up over a 7-year period initialized from WOA13 July-December climatology. We refer to the last 2 years of this simulation, used for analysis below, as the *Bulk Control* (see Fig. 1 for a schematic of the various control and ensemble experiments considered in this study). The forcing input fields used are the atmospheric surface air temperature T_{air}, surface specific humidity q_{air}, sea level pressure P_{air}, zonal and meridional wind stresses τ_x and τ_y, downward solar radiation s_{rad} and downward long-wave radiation l_{rad}. We also use the wind speed magnitude $U_m = \sqrt{U_{10}^2 + V_{10}^2}$ calculated from the 12-hourly ERA-Interim 10m wind speeds U_{10} and V_{10}. The radiative forcing fields include the effects of clouds. For the freshwater forcing we use a relaxation to the WOA13 Sea Surface Salinity (SSS) field with a 10-day relaxation time-scale.

For the majority of simulations discussed in this article we use an Atmospheric Boundary Layer Model (ABLM) to determine the atmospheric air temperature T_{air} and humidity q_{air}, as opposed to specifying them directly as in *Bulk Control*. This is utilized to remove the effective SST nudging associated with a fixed T_{air} (i.e., an infinite atmospheric heat capacity) that restricts the imprint of oceanic internal variability on SST. The implementation of the ABLM used here is based on the cheapAML model of Deremble et al (2013), following earlier work by Seager et al (1995). The model solves single-layer advection-diffusion equations for T_{air} and q_{air} and parameterizes the vertical transfers of heat and moisture at the air-sea interface and the top of the atmospheric boundary layer (see the Appendix for details).

2.3 The Control Ocean Circulation

The *Bulk Control* matches observations well with respect to SST and the equatorial thermal and velocity structure. The SST field (Fig. 2a) shows minimal bias when compared with the 1982 − 2014 ORA-S4 ocean reanalysis product

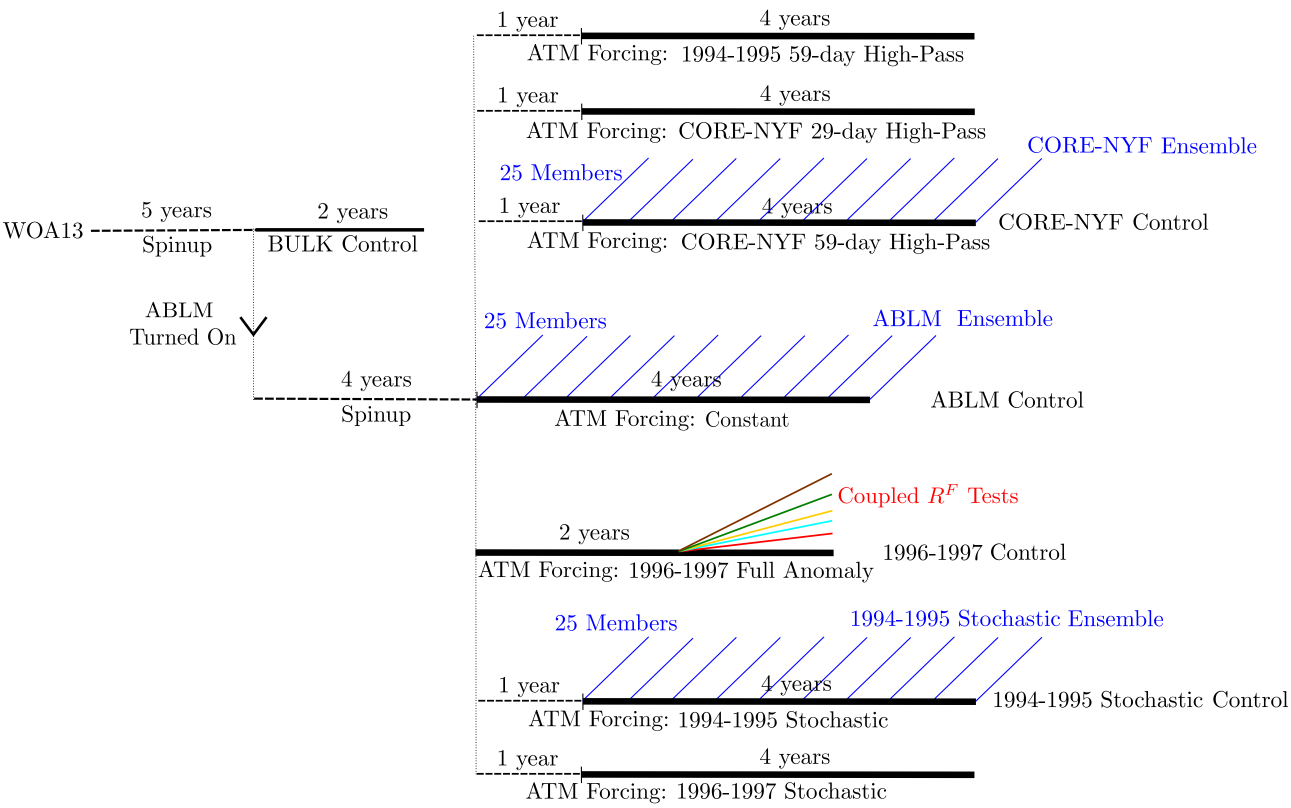

Fig. 1 A schematic illustrating the different control and ensemble experiments considered in this study. A 7 year simulation forced with constant forcing from the ERA Interim 1980-2014 July-December average and using bulk formula is initialized from the WOA13 climatology (left). After 5 years the ABLM is turned on and run for 8 years, with the last 4 years used as *ABLM Control* (thick center black line). *ABLM Control* is used as the initial condition for uncoupled and coupled (see Section 2.5) wind burst experiments, initialized every two months (blue lines - *ABLM Ensemble*). In addition, a range of other control experiments (thick black lines) are produced by adding various estimates of high-frequency atmospheric (ATM) forcing (see Section 2.6). *CORE-NYF Control* and *1994-1995 Stochastic Control* are also used as initial conditions for additional coupled wind burst ensembles (see Figs. 12 and 13 respectively), whose results are compared to the *ABLM Ensemble* (which contains only ocean-sourced variability) to quantify the relative contributions of oceanic and atmospheric variability. We also perform a two-year simulation (*1996-1997 Control*) forced with full atmospheric forcing anomalies from 1996-1997 to evaluate the impact of different coupling coefficients R^F (see Section 4.1).

(Balmaseda et al, 2013) over the July-December season (Fig. 2b). There is a slight 0.5°C cold bias over the central equatorial Pacific and a warm bias reaching 2°C in the far eastern Pacific (associated with common biases in eastern boundary current systems, e.g. Small et al, 2015). The 20°C isotherm depth is too shallow under the ITCZ (by roughly 40m) and the EUC is too strong (by $0.3 - 0.4\text{ms}^{-1}$) and slightly too shallow (not shown). However, the important metrics of the equatorial SST and thermocline depth do not exhibit large biases, and thus the model is sufficient for our purposes.

A simulation with an active ABLM (described in the Appendix) was initialized from the 5th year of the Bulk-forced simulation and run for 8 years. The last 4 years of this simulation, referred to as the *ABLM Control* (see Fig. 1), is used for analysis and as initial conditions for wind burst experiments. There are larger SST biases in this simulation compared to *Bulk Control* (compare Figs. 2d,e to Figs. 2a,b). The 0.5°C cold bias along the equator is slightly more extensive than in *Bulk Control*, while the warm bias in the far eastern Pacific is reduced. There is a 1.5°C warm bias in the western Pacific (Fig. 2e). We expect that the east-west cold-warm bias is mainly a response to the lack of low-cloud feedbacks in the ABLM. In terms of the other fields there are only minimal differences to *Bulk Control*. The upper EUC strength is reduced in *ABLM Control* (Fig. 2f), improving its comparison with the ORA-S4 data (not shown).

In order to study the impact of oceanic internal variability on ENSO it is important to simulate an appropriate level of eddy kinetic energy (EKE). Both *ABLM Control* and *Bulk Control* give similar surface EKE fields, reaching $0.25\text{m}^2\text{s}^{-2}$ in the central Pacific (Figs. 3a,b). These EKE values, which include all time-variable flow in our control simulations, are comparable to observed EKE values (Flament et al, 1996). Isolating only the TIW frequency band, the variance of $3 - 60$ day band-pass filtered meridional velocity at 0°N, 140°N in the upper 50m in *ABLM Control* is $760\text{cm}^2\text{s}^{-2}$, comparable to the $970\text{cm}^2\text{s}^{-2}$ obtained from the TAO array mooring at the same location (calculated using only the months of July-December over the period 2005-2015).

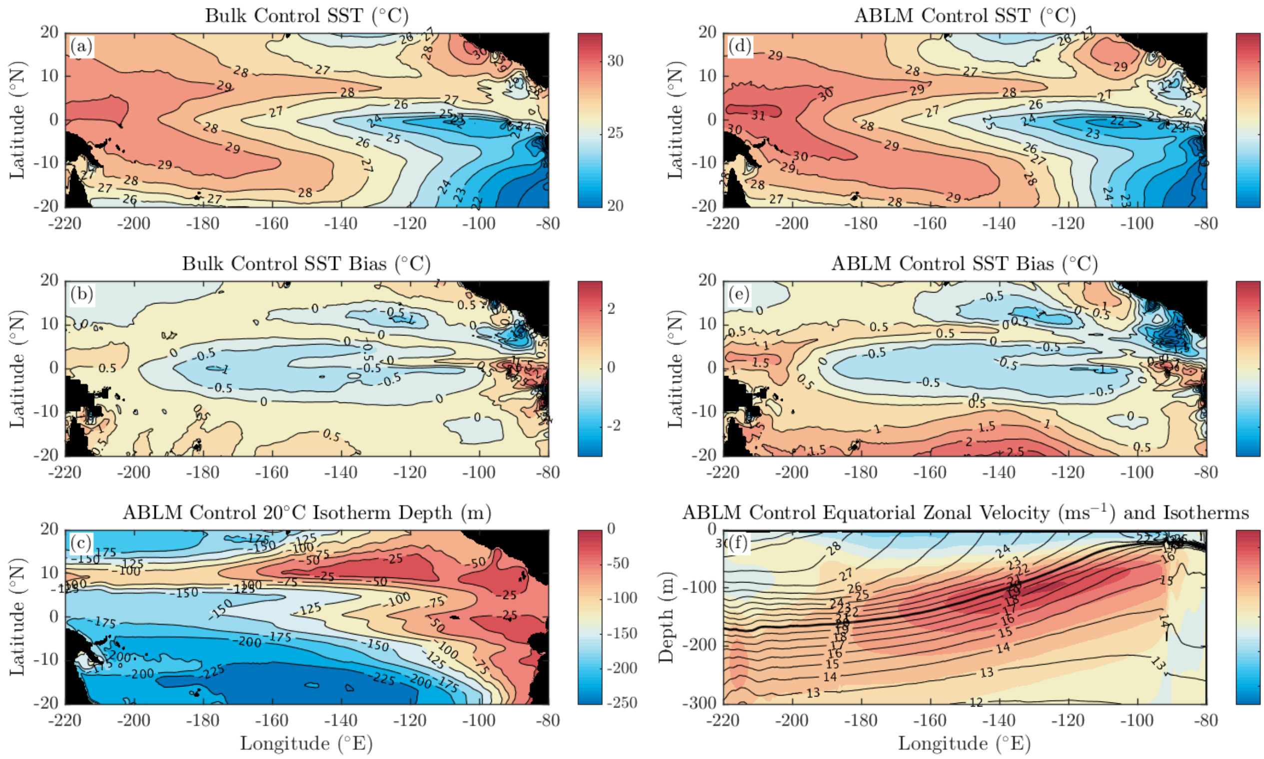

Fig. 2 SST (°C) from (a) *Bulk Control* and (d) *ABLM Control*, averaged over two years. SST bias (°C) compared to the ORA-S4 1980-2014 July-December SST field for (b) *Bulk Control* and (e) *ABLM Control*. (c) 20°C isotherm depth (m) and (f) equatorial depth-longitude slice of zonal velocity (ms^{-1}) and isotherms (°C) from *ABLM Control*.

A spatially-resolved comparison to observations can be made with SSH variability[2] (e.g. Small et al, 2009). A comparison of the 12° longitude high-pass filtered SSH variability between *ABLM Control* and AVISO altimetry observations spanning the period 1993-2016, July-December shows good agreement over the TIW variability peak in the equatorial region (Figs. 3c,d,e east of the dateline between 3°N and 8°N). Therefore we conclude that the model represents the amplitude and spatial distribution of equatorial mesoscale oceanic variability well.

[2] SST could also be used for this purpose. However, this is more strongly influenced by atmospheric variability that is not present in our control simulations.

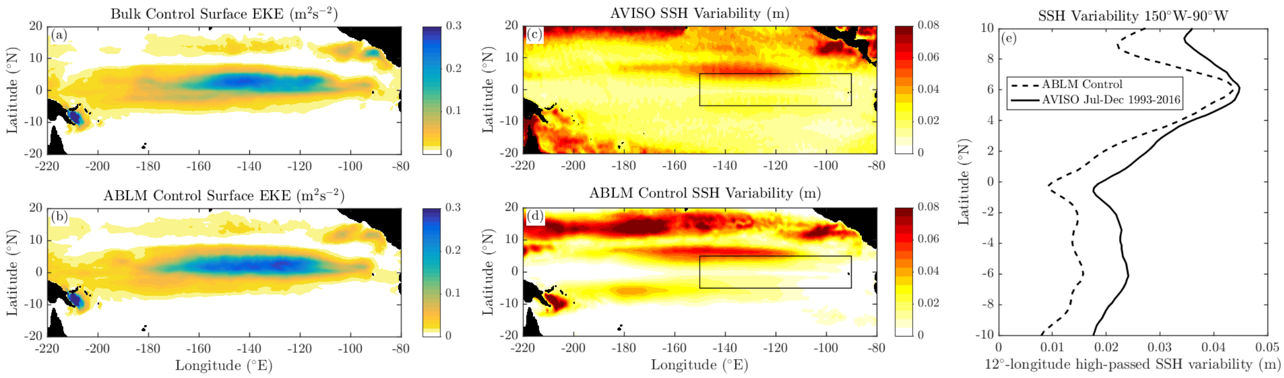

Fig. 3 Surface EKE (m^{2}s^{-2}) from (a) *Bulk Control* and (b) *ABLM Control*, averaged over two years. The EKE is calculated as $\sqrt{(u')^2 + (v')^2}$, where the prime indicates deviations from the temporal mean. Standard deviation of 12°-longitude high-passed SSH variability (m) from (c) AVISO satellite altimetry observations over the period 1993-2016, July-December and (d) *ABLM Control*. (e) SSH variability averaged over the Niño 3 (black box) longitudes 150°W to 90°W for both *ABLM Control* and AVISO.

2.4 Western Pacific Wind Bursts

To examine the role of oceanic internal variability we perform idealized experiments initialized by applying wind bursts over the western Pacific. We use a representative Gaussian wind burst based on the analysis of ERA-40 reanalysis data by Gebbie et al (2007),

$$\tau_x(x, y, t) = A \exp\left(-\frac{(t - t_0)^2}{T^2} - \frac{(x - x_0)^2}{X^2} - \frac{(y - y_0)^2}{Y^2}\right), \tag{1}$$

where $A = 0.07\mathrm{Nm}^{-2}$, $X = 20°$ longitude, $Y = 6°$ latitude and $T = 5$ days. We apply this wind burst centered on the equator ($y_0 = 0°$) at $x_0 = 195°$W. See Gebbie et al (2007) for a discussion of the merits of this choice.

2.5 Statistical Air-Sea Coupling

In addition to uncoupled wind burst experiments, we also perform a series of coupled experiments where the wind stress and other atmospheric variables depend on the oceanic SST anomalies through a statistical relationship. The statistical relationship is based on the first mode of a singular value decomposition (SVD) of the SST and wind stress covariance matrix from the ERA Interim 1980-2014 July-December monthly-averaged data set (Fig. 4a). This first mode represents the dominant mode of air-sea coupling in the region and captures the Bjerknes feedback where a decreased zonal SST gradient across the Pacific leads to a decrease in the strength of the trade winds in the central Pacific. This type of simple coupling has been used extensively in the literature (e.g. Syu et al, 1995; Blanke et al, 1997; Gebbie et al, 2007; Zhang, 2015). We use only one mode because 1) it explains 95% of the covariance in the monthly-averaged July-December SST and wind stress fields, 2) we wish to focus only on the growth phase, not the decay phase of ENSO and 3) the second mode is thought to be closely associated with the seasonal cycle, which is not present in our control forcing. We obtain perturbation fields for the forcing variables other than wind stress by regressing the SVD time-series onto the monthly anomalies of those fields (the patterns for τ_x, τ_y, solar and downward long-wave radiation and wind speed magnitude are shown in Fig. 4b-f). The SVD air temperature and humidity patterns are only used as boundary conditions on the ABLM (i.e., as T_b and q_b in Eqns. (A.1) and (A.2)).

The sequence of steps used while running the coupled model are:

1. Calculate the SST anomaly field ($\mathrm{SST}'(x,y)$) by subtracting the *ABLM Control* SST from the SST field averaged over the last 15 days (and updated every 3 days).
2. Project this SST anomaly onto the SVD mode to obtain the regression coefficient,
$$C = \frac{\sum_{i,j} \mathrm{SST}'_{i,j} \mathrm{SST}^{SVD}_{i,j}}{\sum_{i,j} (\mathrm{SST}^{SVD}_{i,j})^2}, \tag{2}$$
where SST^{SVD} indicates the SST anomaly pattern in Fig. 4a.
3. For each forcing field $F(x,y)$, add the sum of the forcing perturbation fields $F^{SVD}(x,y)$ (e.g. Fig. 4b-f) onto the control forcing $\overline{F}(x,y)$:
$$F(x,y) = \overline{F}(x,y) + CR^F F^{SVD}(x,y), \tag{3}$$

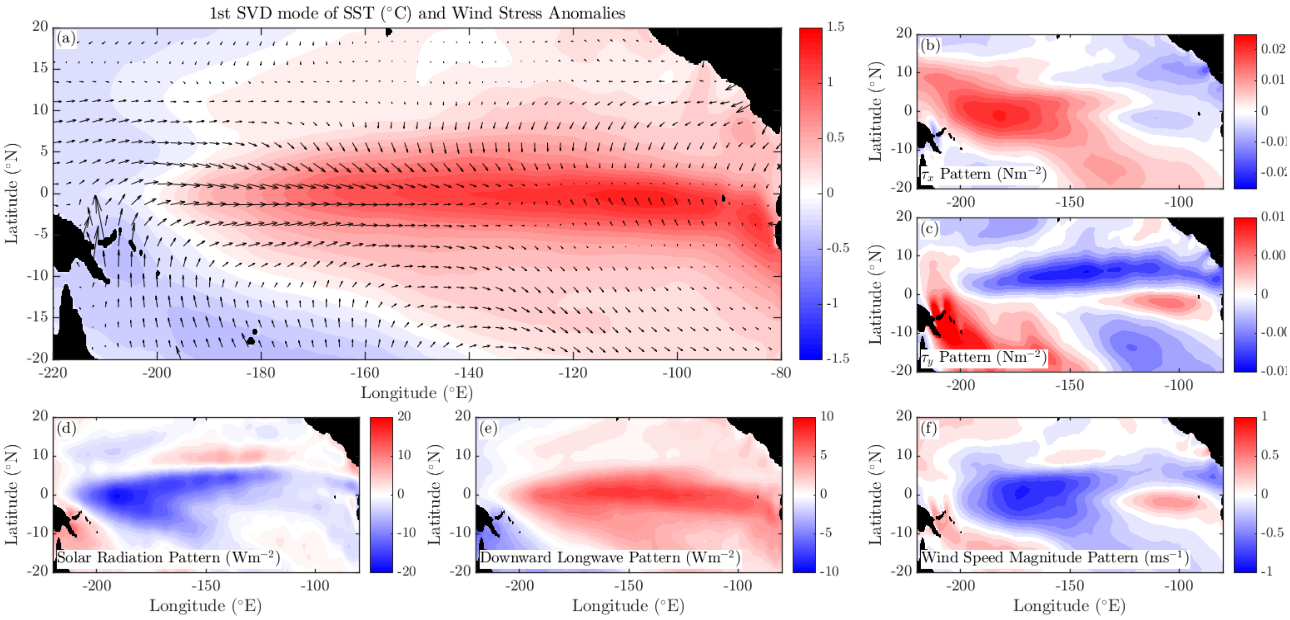

Fig. 4 (a) SST anomaly (°C) and wind stress anomaly vectors for the first SVD mode of SST and wind stress variability in the ERA Interim July-December 1980-2014 data set. The SVD mode time series regressed onto (b) zonal wind stress (Nm^{-2}), (c) meridional wind stress (Nm^{-2}), (d) shortwave radiation (Wm^{-2}), (e) downward long-wave radiation (Wm^{-2}) and (f) wind speed magnitude (ms^{-1}).

where R^F is a coupling coefficient.

The coupling coefficient R^F is an important parameter that can control the growth rate of the coupled system (e.g. Gebbie et al, 2007). We examine results for a range of reasonable coupling coefficients (see Section 4.1).

2.6 Estimates of Atmospheric Internal Variability

In Section 5 we examine how oceanic sourced variability compares with a few different estimates of stochastic atmospheric forcing as described here.

2.6.1 High-pass Filter

One possible method to isolate internal atmospheric variability is to consider only the high-frequency component of atmospheric forcing. For this purpose we use high-pass filtered forcing fields from the Coordinated Ocean-ice Reference Experiment Normal Year Forcing (CORE-NYF, Large and Yeager, 2004) data set. As the CORE-NYF forcing data does not provide wind stress fields, we derive equivalent wind stress fields using the ROMS bulk formula with climatological SSTs from the ORA-S4 reanalysis. These output wind stresses, and the wind speeds, air temperature, humidity and radiation forcing fields from CORE-NYF are then filtered with either a 29-day or a 59-day high-pass filter. Note that we do not include high-frequency forcing on the SSS or atmospheric boundary layer height as this data is not available from CORE-NYF. Note also that we use high-pass forcing from the full CORE-NYF year, not just the July-December season.

This high-frequency forcing is then added on top of the 1980-2014 July-December ERA Interim constant forcing and run for five years (looping over the single CORE-NYF year) initialized from *ABLM Control*. The last four years of this simulation (the *CORE-NYF Control* for the 59-day high pass filter, see Fig. 1) was then used for analysis and as the initial conditions for coupled ensemble runs.

Note that the CORE-NYF forcing set is an estimate of an average climatological year (see Large and Yeager, 2004, for details), and may not, *a priori*, be expected to reproduce accurately the variability associated with wind bursts in the western Pacific. To check whether this influences our results, we also conducted simulations forced with high-pass filtered atmospheric variability from the ERA-Interim data set over the 1994-1995 season (see Fig. 1), chosen for its relatively neutral ENSO state. These results showed little difference in terms of the overall magnitude of variability compared with the CORE-NYF forced simulation (see Section 5).

2.6.2 SVD-based Estimate of Stochastic Atmospheric Forcing

As an alternative to the high-pass filter described in the previous section, we also attempted to directly isolate any atmospheric variability that is apparently independent of the ocean variability. Following Zavala-Garay et al (2003), we construct this stochastic signal by subtracting the component of the atmospheric variability that is captured by the SVD of the wind stress - SST covariance matrix. The SVD is calculated in a similar manner to as in the coupling strategy described in Section 2.5, except here we use the monthly averaged ERA Interim 1980-2014 data for every month of the season (as opposed to just July-December). We use the first three modes to characterize the coupled variability (explaining a total of 98% of the covariance for this time period, 91% in mode 1, 6% in mode 2 and 1% in mode 3), and subtract these modes (multiplied by their time-series) from the ERA Interim daily forcing anomalies. The resulting forcing anomalies do not contain the (linear) modes of the coupled system and thus should represent internal stochastic atmospheric variability that is not associated with oceanic variability. Of course, this method does not remove atmospheric variability that is *non-linearly* related to coupled or oceanic variability, and therefore may possibly overestimate the variability attributed to the atmosphere. A five year simulation with this additional forcing looped over the years 1994-1995, with analysis coming from the last four years (see Fig. 1), was then performed in a similar manner to *CORE-NYF Control* to produce a *1994-1995 Stochastic Control* (see Section 5). This control experiment is also used as initial conditions for a coupled ensemble (*1994-1995 Stochastic Ensemble*). Finally, we also performed a control simulation with stochastic forcing from 1996-1997, which showed similar results to the *1994-1995 Stochastic Control* (see Section 5).

3 Internal Variability in the Uncoupled Simulations

3.1 Internal Oceanic Variability

We first examine the variability in *ABLM Control*, in which ocean-atmosphere coupled feedbacks and atmospheric noise are absent. The SST variability associated with oceanic internal variability is strongest in the eastern equatorial

Pacific, reaching a standard deviation of 1.5°C in a zonal strip surrounding the strong North Equatorial Front associated with TIW induced meridional oscillations of this front (Fig. 5a). Strong variability is also evident throughout the equatorial region east of 200°W, with a higher amplitude north of the equator where both mean meridional temperature contrasts (Fig. 2d) and TIW activity (Fig. 3b) are stronger. This SST variability occurs not only at TIW periods (15-40 days), but also contains a signature at lower-frequencies. The 60-day low-pass filtered SST variability is also peaked in the eastern Pacific, although shows a more homogeneous structure exceeding 0.2°C across much of the equatorial region (Fig. 5b). While this variability is further reduced by averaging over large spatial scales, there is still high and low frequency variability in Niño 3 and Niño 3.4 SST, with anomalies reaching ± 0.2°C (Fig. 5c). This variability, associated purely with oceanic internal variability, is significant relative to the 0.2°C$-$0.6°C SST anomalies associated with typical WWBs and intraseasonal Kelvin waves (Chiodi et al, 2014).

SST variability in the eastern equatorial Pacific is closely related to variability in the thermocline depth, approximated by the 20°C isotherm depth. The 20°C isotherm depth variability is strongest along 5°N as a consequence of the strong TIW activity there (Fig. 5d). However, again there is still variability in the thermocline depth at frequencies slower, and scales larger, than the TIWs (Fig. 5e), with variations of ± 2m averaged over the Niño 3 and Niño 3.4 regions (Fig. 5f). These low frequency and large spatial scale anomalies are a consequence of the nonlinear rectification of eddy-driven variability (e.g. Penduff et al, 2011; Arbic et al, 2014). Deep (shallow) Niño 3 20°C isotherm depth anomalies lead warm (cold) Niño 3 SST anomalies by 39 days with a correlation coefficient of 0.49. This connection is weaker in the Niño 3.4 region where the mean thermocline is deeper (Zelle et al, 2004).

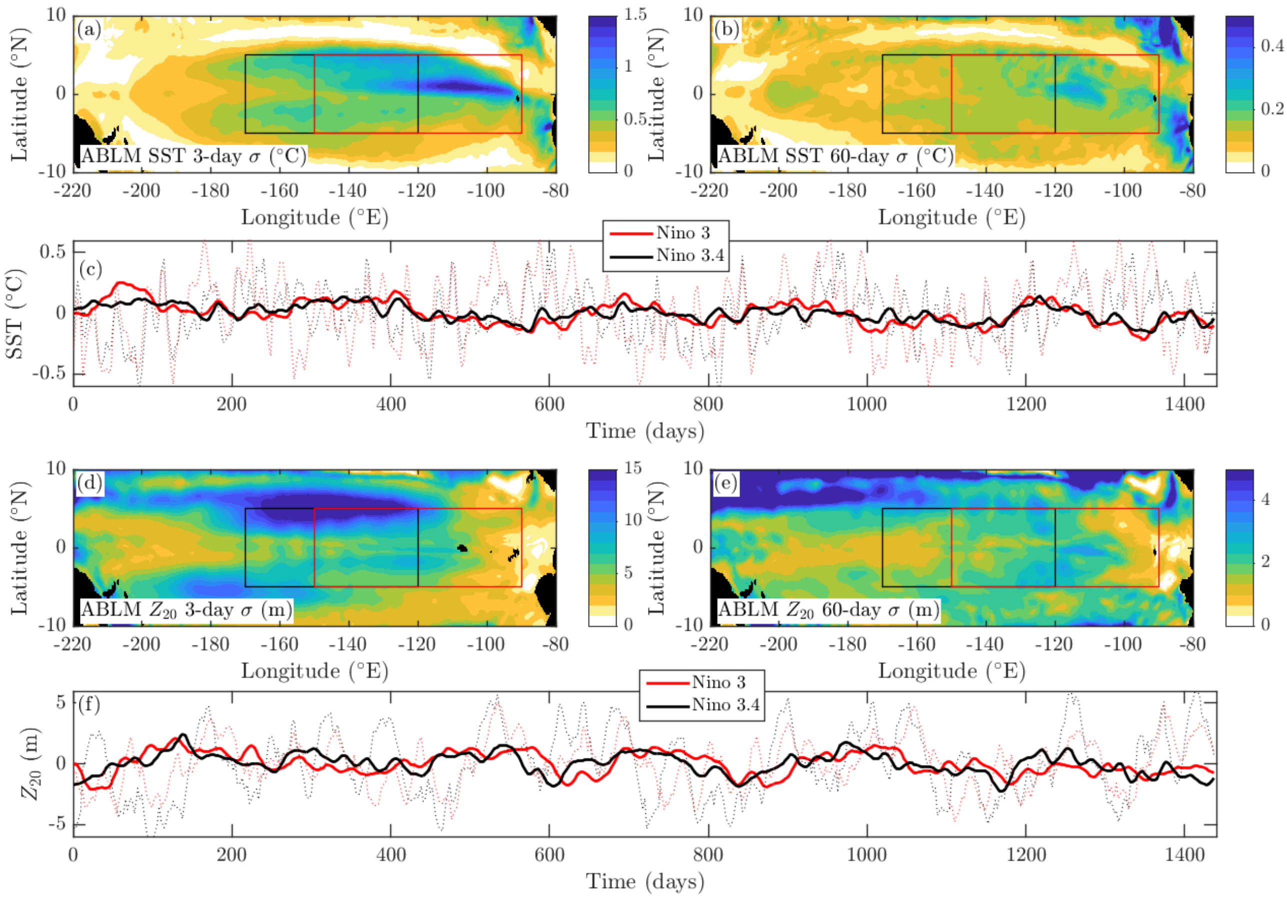

Fig. 5 Variability in *ABLM Control*. Standard deviation of (a) the 3-day averaged model output SST (°C) and (b) 60-day low-pass filtered SST (°C). (c) Time series of Niño 3 and Niño 3.4 SST anomalies (°C). Standard deviation of the 20°C isotherm depth (m) from (d) the 3-day averaged model output and (e) 60-day low-pass filtered data. (f) Time series of Niño 3 and Niño 3.4 20°C isotherm depth anomalies (m). The thin dotted lines in (c) and (f) show the results from a simulation with additional 59-day high-pass CORE-NYF atmospheric variability added (*CORE-NYF Control*, discussed in Section 5).

3.2 The response of the ocean to a wind burst

We now examine the response of the ocean to idealized western Pacific wind bursts. We apply Gaussian WWBs [Eq. (1)] and Easterly Wind Bursts [EWBs, obtained by changing the sign of A in Eq. (1)] over an ensemble of simulations which capture the spread across the internal variability of *ABLM Control*. We construct 25 ensemble members in each set by imposing wind bursts at the beginning of every consecutive two-month period over the four years of *ABLM Control*. Averaged over the 25 ensemble members, the WWB creates a downwelling Kelvin wave that travels across the Pacific basin in $\sim$100 days, evident in anomalies of the 20°C isotherm depth (contours in Fig. 6a-c and color in Fig. 6f). The Kelvin wave creates warm SST anomalies in the central and eastern Pacific through both the changes in thermocline depth and zonal advection (color in Fig. 6a-d and Fig. 6e). These SST anomalies develop somewhat after the thermocline depth anomaly of the Kelvin wave, consistent with the delay expected from zonal advection and the impact of thermocline depth anomalies on SST (compare color in Figs. 6e and 6f, also see Zelle et al (2004)). These SST anomalies are strongest along the equator east of 140°W, and are reduced north of the equator, which may be due to the TIW activity there (Holmes and Thomas, 2016). The downwelling Kelvin wave is also followed by a weaker upwelling wave that shoals the thermocline and cools the sea surface.

The WWB also creates a strong warm SST anomaly in the western Pacific between 200°W and 180°W through zonal advection of a background zonal SST gradient in this region (Fig. 2d). This warm SST anomaly is larger than observations may suggest as the background SST and SST gradient are biased in this region (Fig. 2e). However, this enlarged response is unlikely to affect the results of this study for several reasons; 1) The amplitude of the SST SVD pattern is weak in this region (Fig. 4a), meaning that the statistical atmosphere responds only weakly to SST anomalies here. 2) Any amplified response of the atmosphere to SST anomalies in this region is absorbed into the coupling coefficient choice (Section 4.1). Most importantly, 3) if the atmosphere does respond to overly large SST anomalies in this region then the influence of oceanic internal variability on the trajectory of the coupled system will be underestimated, not overestimated, as oceanic internal variability is relatively weak here.

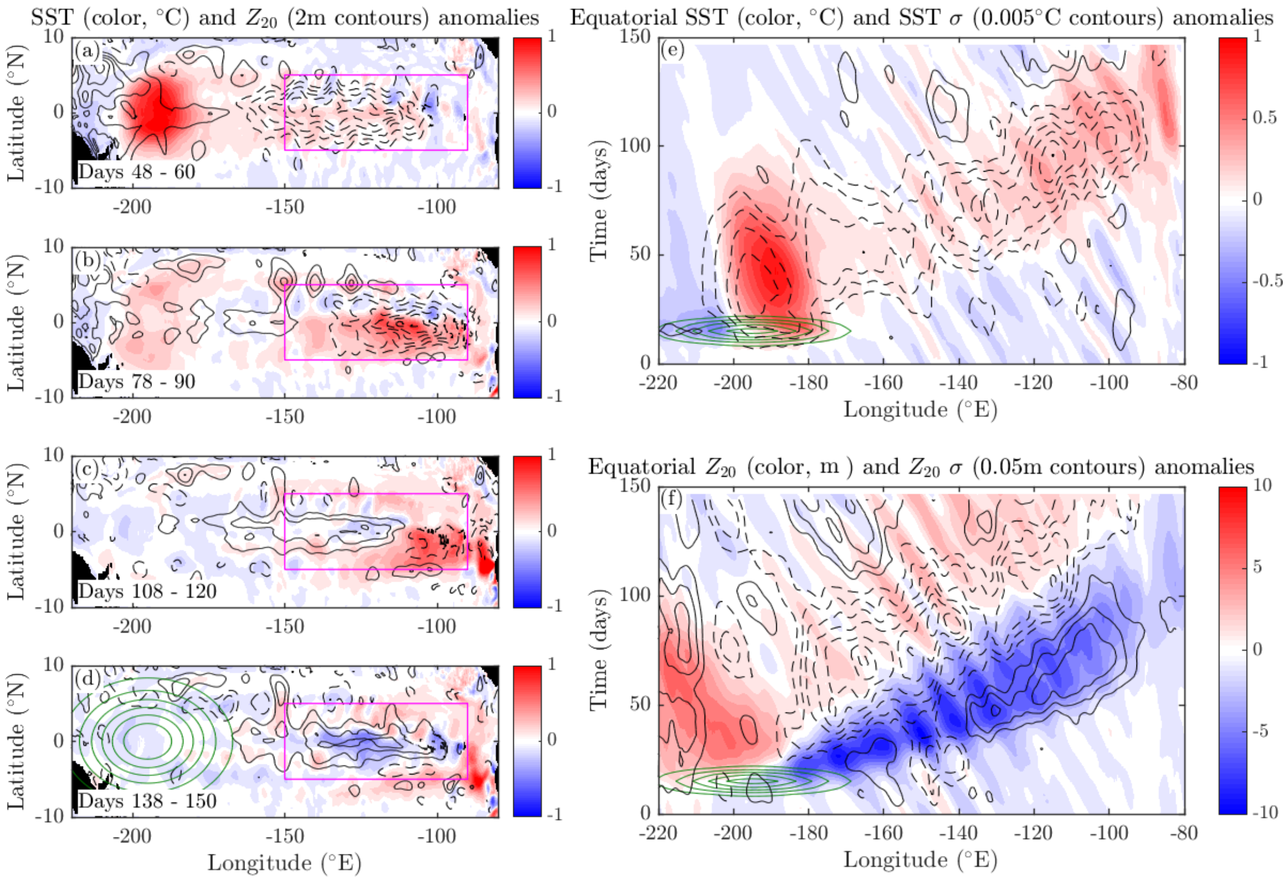

Fig. 6 The uncoupled response of the *ABLM Control* simulation to a WWB applied in the western Pacific (with spatial structure shown with green contours in d), averaged over 25 ensemble members. (a-d) Spatial pattern of SST anomalies (°C, color), where the solid (dashed) contours show positive (negative) Z_{20} anomalies at 2m intervals. A positive (negative) Z_{20} anomaly indicates an anomalously shallow (deep) thermocline. The magenta box shows the Niño 3 region. Longitude-time plots of (e) SST (°C) and (f) Z_{20} anomalies (m) averaged between ±5° latitude. Solid (dashed) contours show where the standard deviation of the variability across the ensemble members is enhanced (decreased), with 0.005°C intervals for SST and 0.05m intervals for Z_{20}.

The western Pacific WWB (in the absence of coupling) leads to a 0.25°C peak warm anomaly within the Niño 3 region (black thick line in Fig. 7a), occurring 36 days after the peak Niño 3 Z_{20} anomaly (black thick line in Fig. 7b) and 81 days after the WWB peak. However, there is large spread across the ensemble members, particularly in SST, with Niño 3 anomalies between 0.12°C and 0.4°C possible across the 95% confidence interval due to oceanic internal variability (gray shading in Fig. 7a, estimated at each time using a non-parametric bootstrap). The EWB ensemble produces a corresponding cool Niño 3 anomaly (blue lines and shading in Fig. 7a). The spread of SST variability across the EWB ensemble is slightly larger than that in the WWB ensemble (see Table 1) likely associated with an increase in the EKE of the TIW field (Fig. 7c) in response to the Kelvin wave. These statistics are summarized in Table 1. The enhancement in EKE for the EWB compared to the WWB occurs as a consequence of changes in the background flow induced by the Kelvin wave which alter the TIW kinetic energy balance, as discussed by Holmes and Thomas (2016). These changes also act to damp the SST anomalies associated with the Kelvin waves, which would be larger if the TIWs were absent (Holmes and Thomas, 2016). Nevertheless, it is clear that the oceanic internal variability impacts both the magnitude and duration of the SST response to the wind burst. This implies that the coupled ocean-atmosphere system may respond differently to a given WWB depending on the phase of the internal oceanic variability, as we explore in the next section.

4 The Role of Oceanic Internal Variability in a Coupled System

In this section, we examine the influence of oceanic internal variability on the evolution of a simple coupled ocean-atmosphere system. Here, in contrast to the previous section, the wind stress and other atmospheric variables are allowed to vary depending on the SST anomalies of the ocean model through the single-mode SVD statistical relationship discussed in Section 2.5. We first discuss the choice of the coupling coefficient using simulations initialized with historical forcing anomalies leading up to the 1997-1998 El Niño (Section 4.1) and then discuss the influence of oceanic internal variability on the variability in the forecast amplitude of events initiated by WWBs (Section 4.2).

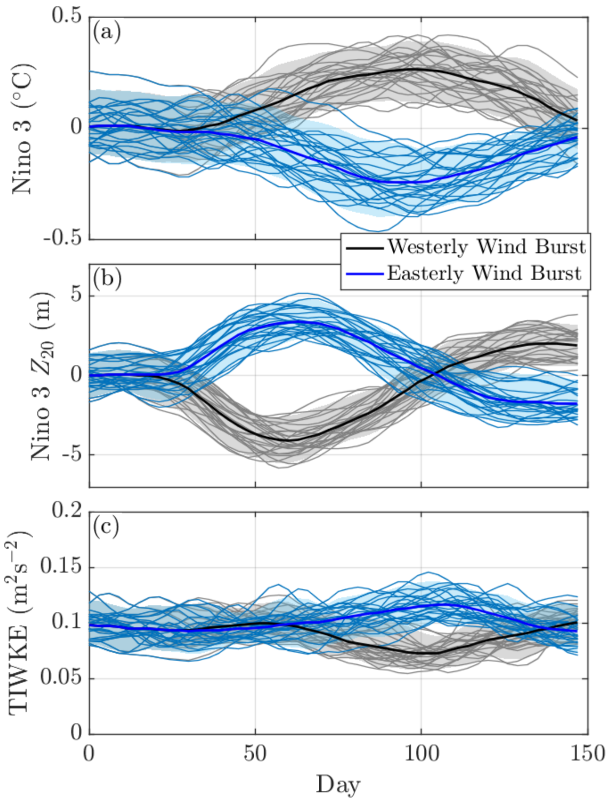

Fig. 7 (a) Niño 3 SST (°C), (b) Niño 3 Z_{20} (m) anomalies and (c) eastern Pacific surface EKE (m^2s^{-2}, averaged between 7°S and 10°N, 150°W and 110°W) in response to a WWB (gray) and an EWB (blue). Individual ensemble members are shown with thin lines. Also shown are the ensemble mean (solid line) and 95% confidence interval (shaded) determined using a non-parametric bootstrap over all 25 ensemble members at each time.

4.1 The choice of coupling coefficient R^F

In order to evaluate the performance of the SVD coupling method, and choose a coupling coefficient R^F, we examine a set of simulations based on the 1997-1998 El Niño. We choose the 1997-1998 event case as it is the strongest El Niño on record with robust air-sea coupling. We first perform an uncoupled simulation over 1996 and 1997, leading up to the event. As our control simulation does not contain a seasonal cycle, we perform an anomaly forced simulation, where the 1980-2014 climatology of the ERA Interim forcing is subtracted

Table 1 A summary of the Niño 3 SST anomalies and their spread due to oceanic internal variability in the various sets of ensemble simulations. The columns indicate the control simulation, the type of wind burst applied, the statistical coupling coefficient, the period over which the statistics are measured, the ensemble mean Niño 3 SST anomaly (°C), the ensemble spread of Niño 3 SST anomalies (°C) and the ratio of the ensemble spread to the ensemble mean Niño 3 anomaly respectively. Every ensemble contains 25 members. The ensemble spread is quantified as half of the range of the 95% confidence interval determined using a non-parametric bootstrap using 2000 random bootstrap samples of the 25 ensemble members averaged over the given time interval. Within each bootstrap sample the 2.5% and 97.5% quantiles are calculated based on the rank ordering within the sample. The numbers in brackets represent the 95% confidence interval of the given statistic from the bootstrapping.

Control	Wind Burst	R^F	Day	Niño 3 Mean (°C)	Niño 3 Spread (°C)	Spread / Mean
Uncoupled Experiments						
ABLM	WWB	0.0	96	**0.26** (0.23, 0.29)	**0.14** (0.10, 0.17)	0.51
ABLM	EWB	0.0	96	**-0.24** (-0.28, -0.21)	**0.16** (0.13, 0.18)	0.63
Coupled Experiments						
ABLM	2 WWBs	0.9	198-258	**0.61** (0.55, 0.67)	**0.26** (0.17, 0.34)	0.42
ABLM	2 WWBs	1.0	198-258	**0.81** (0.73, 0.90)	**0.34** (0.25, 0.44)	0.42
ABLM	2 WWBs	1.1	198-258	**1.05** (0.93, 1.17)	**0.47** (0.34, 0.60)	0.45
ABLM	2 EWBs	1.0	198-258	**-0.63** (-0.71, -0.55)	**0.34** (0.24, 0.43)	0.54
CORE-NYF 59-day	2 WWBs	1.0	198-258	**0.67** (0.55, 0.78)	**0.47** (0.38,0.55)	0.70
1994-1995 Stochastic	2 WWBs	1.0	198-258	**0.56** (0.03, 1.09)	**1.91** (1.69, 2.12)	3.41

from the 1996-1997 period, and then these forcing anomalies are added back onto the July-December *ABLM Control* forcing. *1996-1997 Control* thus contains the influence of sub-seasonal variability, such as the strong WWBs that occurred in January and March of 1997 (west of 180°E in Fig. 8a), and the interannual anomalies but not the seasonal cycle. These two WWBs initiate strong downwelling equatorial Kelvin waves which deepen the thermocline in the eastern Pacific (Fig. 8b) and condition the system for the growth of the 1997-1998 El Niño event.

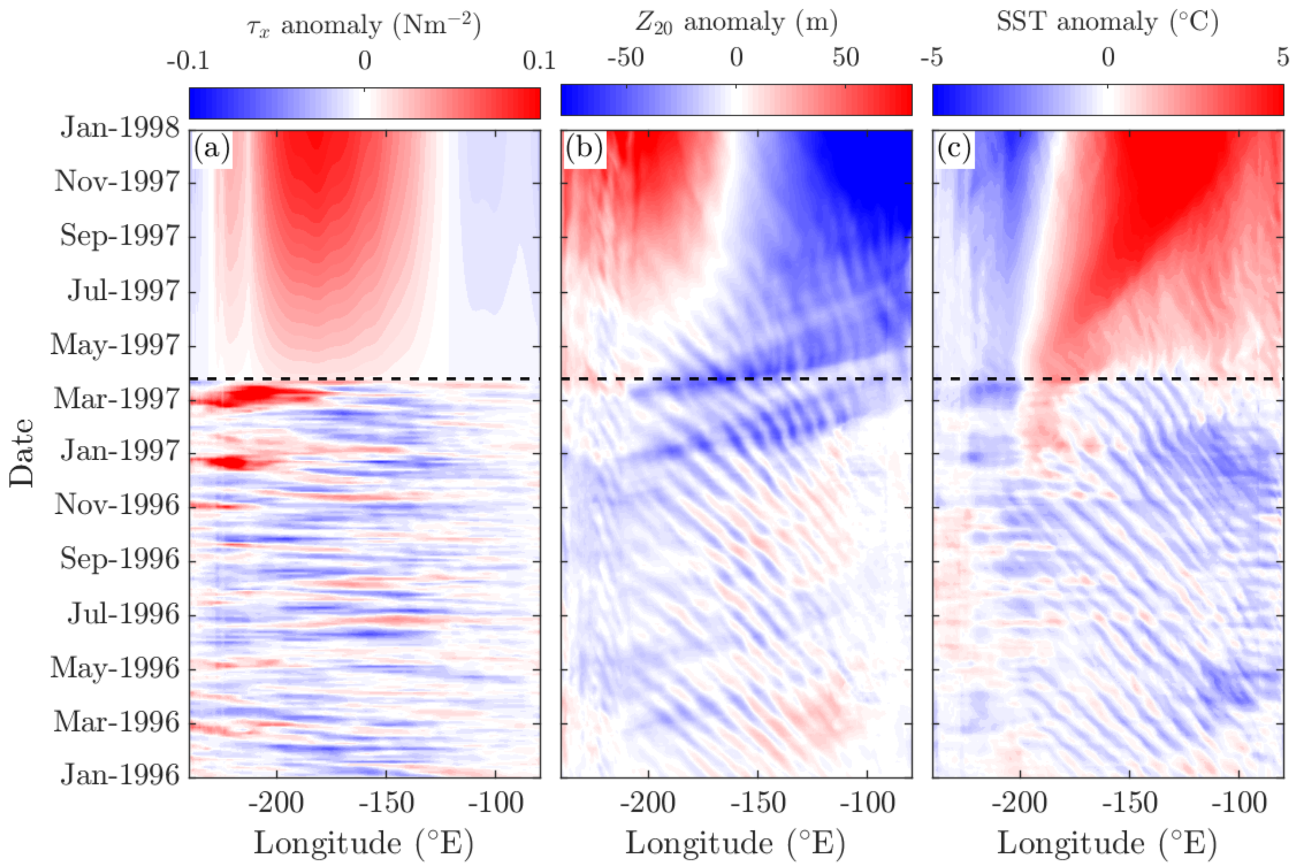

Fig. 8 (a) Zonal wind stress (Nm^{-2}), (b) Z_{20} (m) and (c) SST (°C) anomalies from a simulation forced with observed anomalous forcing from 1996 and 1997. On the 26th of March 1997 (black dashed line) the anomalous forcing is turned off and the simple statistical coupling is turned on, with a coupling coefficient $R^F = 1.0$.

The intention of this anomaly forced simulation is to initialize the system in a state prone to the development of an El Niño (e.g. as at the end of March 1997), and then see if the SVD coupling can capture the growth of the event. We therefore perform a coupled SVD simulation initialized from *1996-1997 Control* on March 26th 1997 (see Fig. 8). From this point onward, the forcing is determined from the *ABLM Control* background forcing and the SVD perturbed forcing, that depends on the current state of the SST anomalies (averaged over the previous 15 days). Due to the equatorial Kelvin waves initiated by the WWBs prior to March 26th, the eastern Pacific SST warms (Fig. 8c). The wind stress in the western Pacific then weakens (Fig. 8a) through its statistical dependence on the central and eastern Pacific SST, driving further changes in the thermocline depth (Fig. 8b) that amplify the initial perturbations. This leads to the growth of an El Niño event and the development of warm SST anomalies in the vicinity of 5°C in the central and eastern Pacific by the end of 1997. We are therefore successful in capturing the first-order dynamics of the coupled system in the growth phase of an El Niño. Due to the simple coupling method and lack of seasonal cycle some of the details of the observed event are not captured. The spatial structure of the wind stress anomalies are fixed, while in reality the wind stress anomalies shift eastward as the event grows. As a consequence, the SST anomalies are shifted westward relative to observations. Note also that this system does not capture the decay phase of the event, as the lack of a seasonal cycle and the use of only one SVD mode does not capture, for example, the southward shift of wind anomalies thought to be critical for triggering decay (e.g. McGregor et al, 2013; Abellán and McGregor, 2015).

The growth rate of the El Niño depends on the coupling coefficient included in the SVD statistical relationship [R^F in Eq. (3)]. To evaluate the impact of this choice, we perform simulations with coupling coefficients ranging from 0.8 to 1.25, all initialized from *1996-1997 Control* on the 26th of March 1997. All of these simulations capture a growing eastern Pacific SST anomaly (colored lines in Fig. 9a) coupled with a growing western Pacific zonal wind stress anomaly (colored lines in Fig. 9b). While it is difficult to objectively decide on which coupling coefficient produces the most realistic growth, 0.9, 1.0 and 1.1 all agree reasonably well with the growth rate of the *1996-1997 Control* (black solid line in Fig. 9) and the observed (black dashed line in Fig. 9a) Niño 3 anomalies. The 0.8 simulation (red line in Fig. 9) grows much more slowly than the others, and the 1.25 simulation (brown line in Fig. 9) grows much more quickly, and peaks well before the *1996-1997 Control* SST peak. We thus examine coupling coefficients within the range $0.9 - 1.1$. However, in the next

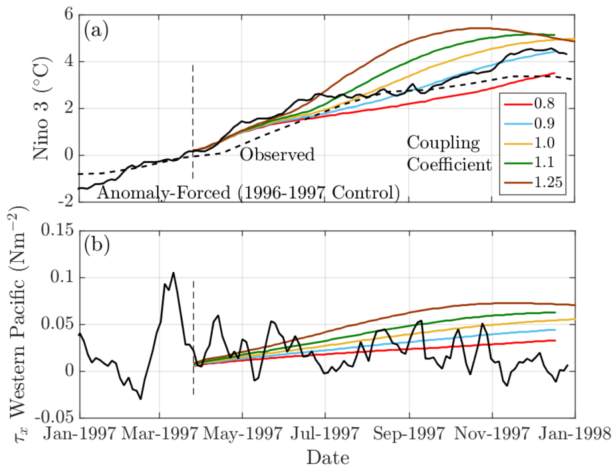

Fig. 9 Coupled simulations based on the lead up to the 1997-1998 El Niño as a test of the coupling coefficient included in the simple statistical coupling. (a) Niño 3 SST (°C) time series over 1997. The dashed black line shows the observed Niño 3 SST anomalies for 1997. The solid black line shows the Niño 3 SST anomaly for 1997 from *1996-1997 Control* forced with wind stress and other atmospheric forcing anomalies from 1996-1997. *1996-1997 Control* is used as an initial condition for five coupled runs that are initialized on the 26th of March 1997 (vertical dashed line), with a range of different coupling coefficients (colored lines). (b) western Pacific zonal wind stress (Nm^{-2}, averaged between 10°S and 10°N, 140°E and 180°E) corresponding to (a).

section we find that the relative impact of oceanic internal variability on the coupled system is not sensitive to this choice.

4.2 Coupled WWB ensembles

We now perform a series of ensemble coupled forecast experiments initialized from different states taken every two months from *ABLM Control* (Fig. 10). Similar to the uncoupled ensemble simulations (Fig. 7), we initialize each simulation by applying external western Pacific wind bursts [from Eq. (1)] to prime the coupled system for growth. To obtain realistic growth with coupling coefficients of $0.9 - 1.1$, we found it was necessary to apply two WWBs separated by 35-days. This is for several reasons, including the lack of anomalous warm water volume (WWV) build-up prior to the WWBs in our experiment design (e.g. see Fedorov et al, 2015), and the relatively weak idealized Gebbie et al (2007) wind burst, which has roughly 1/4 the peak strength of the March 1997 wind burst as measured by western Pacific wind stress anomalies averaged over 10°S-10°N, 140°E-180°E (compare Fig. 10c and Fig. 9c). The warm SST anomalies in the eastern Pacific, that result from the WWBs and subsequent equatorial Kelvin waves (e.g. see Fig. 6), amplify with time at a rate dependent on the coupling coefficient (compare blue, red and black lines in Fig. 10a). However, there is significant spread amongst the ensemble members (shaded confidence intervals in Fig. 10), which highlights the prominent role of oceanic internal variability. This spread increases with coupling coefficient.

As mentioned above the single-mode SVD coupling does not capture the decay phase of ENSO, resulting in sustained growth. To quantify the impact of oceanic internal variability on the amplitude of coupled events we therefore focus on a period $5-7$ months after the peak of the second WWB. This is appropriate, for example, to examine the variability near the end of the year for WWBs occurring at the end of June. Over this time period (indicated by a bar in Fig. 10a), the Niño 3 anomaly ranges from 0.5°C to 1.2°C over the 95% confidence interval across ensemble members for a coupling coefficient of 1.0. This ±0.34°C spread in the response is significantly greater than the ±0.14°C variability in the uncoupled case (Fig. 7). These statistics are summarized in Table 1. The spread is sensitive to the coupling coefficient, with a smaller spread of ±0.27°C for a coupling coefficient of 0.9 (although this is still significantly enhanced above the uncoupled variability) and a larger spread of ±0.47°C for a coupling coefficient of 1.1. However, across these different coupling coefficients oceanic internal variability accounts for a consistent spread of approximately ±45% the size of the ensemble mean Niño 3 response six-months after the second WWB (last column of Table 1). This indicates that oceanic internal variability may contribute to the stochastic forcing of the ENSO cycle and potentially degrade the skill of ENSO predictions that do not capture this internal variability.

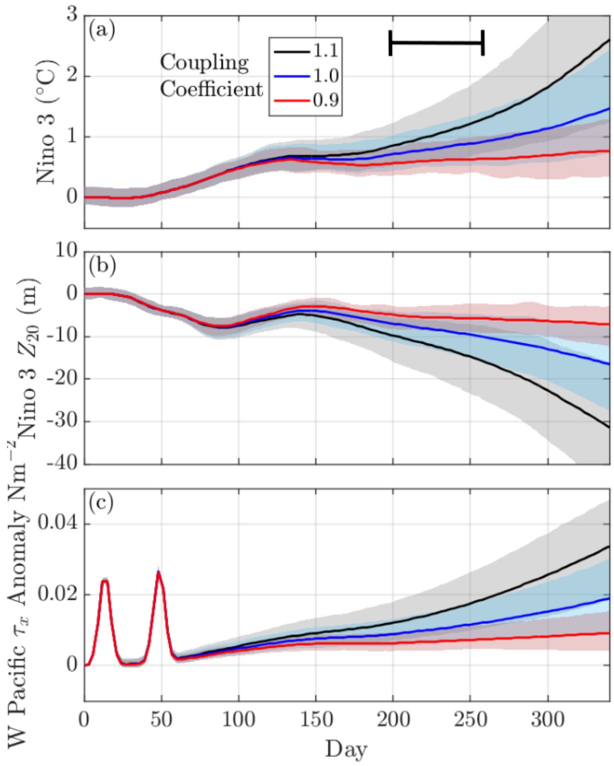

Fig. 10 Ensemble coupled runs initiated from *ABLM Control* with three different coupling coefficient $R^F = 0.9$ (red), 1.0 (blue) and 1.1 (black). (a) Niño 3 SST (°C), (b) Niño 3 Z_{20} (m) anomalies and (c) western Pacific zonal wind stress (Nm^{-2}, averaged between 10°S and 10°N, 140°E and 180°E). The ensemble mean is shown with the solid line and the 95% confidence interval calculated using a non-parametric bootstrap is shown with the shading. The black dashed bar in (a) marks the time period 5-7 months after the peak of the second WWB, where statistics are collated in Table 1.

We also conducted a series of coupled ensemble forecast experiments initialized with two EWBs instead of WWBs (not shown). These experiments showed similar ensemble spread as the WWB experiments, however, the ensemble mean Niño 3 anomaly was negative, and somewhat smaller than in the WWB experiments (see Table 1). This suggests that there is an asymmetry between La Niña and El Niño events in our idealized coupled setup. Since the wind stress responds linearly to SST anomalies this asymmetry is likely sourced in the ocean (although there are some non-linearities in the surface heat fluxes). A careful examination of the sources of this asymmetry is outside the scope of this article and will be left to future work. However, variations in TIW EKE and lateral heat fluxes are likely to play a role (An, 2009; Imada and Kimoto, 2012; Holmes and Thomas, 2016).

5 How does the oceanic variability compare to atmospheric variability?

In the previous section we showed that internal oceanic variability can drive variability in the response of our coupled system to a given series of wind bursts. Here, we examine how this oceanic-sourced variability may compare with variability sourced from internal atmospheric processes.

5.1 High-pass filtered atmospheric variability

We begin by considering *CORE-NYF Control*, which, in addition to the oceanic internal variability, contains high-frequency atmospheric variability from a 59-day high-pass filter of the CORE-NYF data set, as described in Section 2.6. Frequency spectra of this added wind stress forcing in the western Pacific show a relatively white spectrum at frequencies above the 59 day cutoff, with a rapid decay at lower frequencies (thick blue dashed line in Fig. 11a). This additional high-frequency variability in wind stress, as well as in the other atmospheric forcing fields, induces high-frequency variability in Niño 3 and Niño 3.4 SST that has an order of magnitude more variance at periods shorter than ~ 90 days than *ABLM Control* (compare black and thick blue dashed line in Fig. 11b, also compare the time series of Niño 3 and Niño 3.4 SST, dashed lines in Fig. 5c). However, there is only a somewhat smaller boost to the high-frequency variability in the thermocline depth (compare black and thick blue dashed line in Fig. 11c, also compare the time series of Niño 3 Z_{20} and Niño 3.4 Z_{20}, dashed lines in Fig. 5f). This suggests that much of the additional variability coming from the atmosphere in *CORE-NYF Control* is

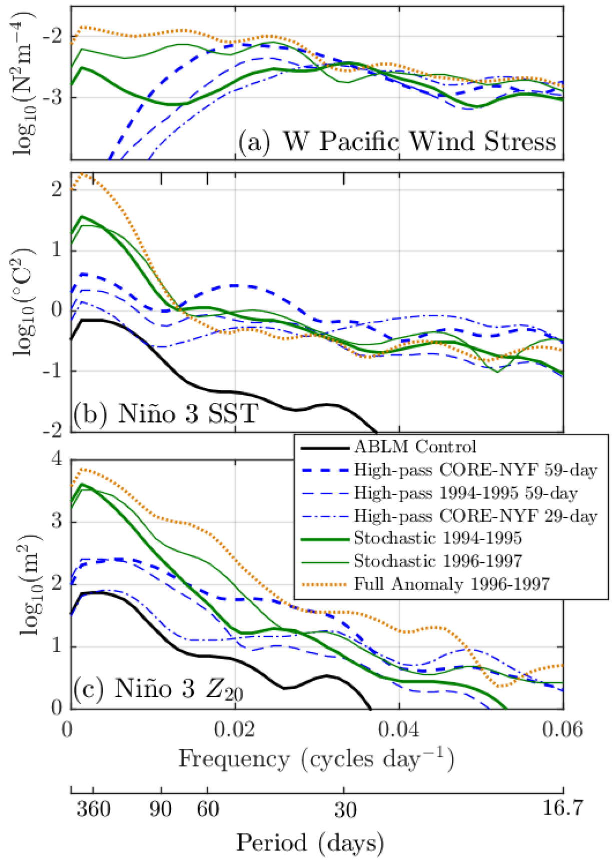

Fig. 11 Welch power spectra of (a) western Pacific wind stress (averaged between 10°S and 10°N, 140°E and 180°E), (b) Niño 3 SST and (c) Niño 3 Z_{20} from the various control simulations including *ABLM Control* with no atmospheric variability (black solid), with additional high-pass filtered atmospheric variability (blue dashed lines), with additional stochastic atmospheric variability estimated as described in Section 2.6 (green solid lines) and from *1996-1997 Control* with full atmospheric forcing anomalies over the 1996-1997 period (yellow dotted lines). All spectra are calculated from four-year periods except for *1996-1997 Control* which is two years. Note that the y-scales of each of the three subplots are the same to facilitate comparison of the range of variability magnitudes between variables.

through variations in the air-sea heat flux that influence the temperature in the mixed-layer, as opposed to variability in the wind stresses impacting the thermocline depth through wind-stress curl and remotely forced equatorial waves.

Despite the drop-off in the wind stress spectra at periods below 90 days, there is still a boost in the low frequency variability of both SST and thermocline depth (compare black and thick blue dashed lines at periods below 90 days in Fig. 11b,c). Note that an additional control simulation forced with 59-day high-pass filtered ERA Interim forcing over the 1994-1995 period (looped to produce a four-year control simulation, see Fig. 1) gives a similar, if slightly smaller, level of variability to *CORE-NYF Control* (compare thick and thin blue dashed lines in Fig. 11). Also, using a 29-day high-pass cutoff instead of a 59-day high-pass cutoff produces less low frequency variability as expected (compare thin dot-dashed and thick blue dashed lines in Fig. 11). In this case, the low frequency variability in SST and Z_{20} is mostly associated with purely oceanic-intrinsic processes (compare blue dot-dashed and black lines in Fig. 11b,c).

The additional variability coming from the 59-day high-pass CORE-NYF forcing is likely to enhance the ensemble spread in the trajectory of the coupled forecasts. To test this, we conduct additional ensemble forecast experiments, referred to as the *CORE-NYF Ensemble*, with the CORE-NYF high-frequency forcing and initiated from *CORE-NYF Control* (see Fig. 1). To compare to the *ABLM Control* coupled experiments (Fig. 10), we maintain the same experimental design initiating each experiment with two WWBs. We use a coupling coefficient of $R^F = 1.0$. Initially the Niño 3 SST ensemble spread is $2-3$ times larger in the *CORE-NYF Ensemble* than in the *ABLM Ensemble* (compare blue and gray confidence intervals at day 0 in Fig. 12a). Previously, we have seen that the coupling enhances the ensemble spread as the coupled anomalies grow. However, the growth in the ensemble spread in Niño 3 in the *CORE-NYF Ensemble* is minimal, reaching $\pm 0.47°$C $5-7$ months following the second WWB and exceeding that in the *ABLM Ensemble* ($\pm 0.34°$C) by a factor of only 1.4 (see Table 1). This is likely because the impact of the high-frequency forcing on the thermocline depth is more muted than its direct influence on SST, and it is this variability in the thermocline depth that can lead to more sustained SST anomalies. The high-pass filtered CORE-NYF western Pacific

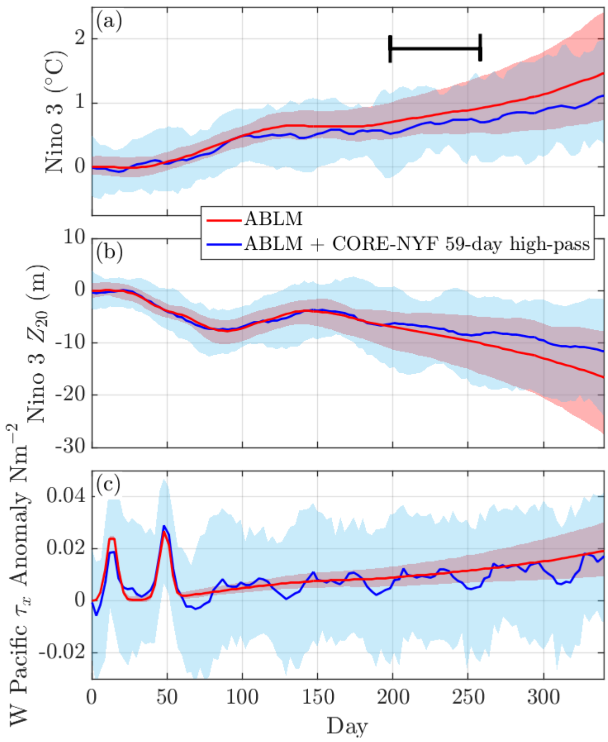

Fig. 12 As for Fig. 10 except comparing the results of two WWB coupled experiments (with coupling coefficient $R^F = 1.0$) with (blue) and without (black) additional CORE-NYF 59-day high-pass atmospheric forcing.

wind stress variability is unable to create sustained large-amplitude equatorial waves that have a strong signature in eastern Pacific thermocline depth.

In conclusion, in this idealized experimental setup with high-frequency atmospheric variability we find that the oceanic internal variability provides much of the variability in forecast event amplitude. If we take the *ABLM Ensemble* spread as representative of the oceanic internal variability, which is also present in the *CORE-NYF Ensemble*, then in the *CORE-NYF Ensemble* 72% of the $5 - 7$ month Niño 3 ensemble spread is associated with oceanic internal variability.

5.2 Stochastic estimate of atmospheric variability

One reason that the oceanic internal variability contributes more than atmospheric variability to the spread in forecast amplitude in the *CORE-NYF Ensemble* may be because the use of a high-pass filter effectively removes all of the low frequency atmospheric forcing (e.g. Fig. 11a at periods longer than 90 days). Some of the removed signal could potentially be associated with the low frequency tail of stochastic internal atmospheric variability (Levine and Jin, 2017). Therefore, we also consider surface forcing derived using the SVD method discussed in Section 2.6.2 which isolates the component of atmospheric variability that is apparently independent (or at least not linearly-dependent) on the ocean or coupled variability. We performed two additional control simulations with added stochastic forcing taken from the periods 1994-1995 and 1996-1997. Each of these simulations was run for five years (looping over the 1994-1995 and 1996-1997 periods), initialized from *ABLM Control*, with analysis here coming from the last four years (see Fig. 1). The wind stress forcing associated with these experiments contains a similar level of high-frequency variability as the high-pass filtered cases, but does not decay at low frequencies (compare green solid and blue dashed lines in Fig. 11a). Correspondingly, there is around an order of magnitude more variance at low frequencies in both Niño 3 SST and thermocline depth (compare green solid and blue dashed lines in Fig. 11b,c at periods below 90 days). Note that the 1996-1997 period has a higher level of low frequency wind stress variability, but similar levels of low frequency SST and thermocline depth variability (compare green thin and thick lines in Fig. 11a).

The enhanced low-frequency variability under the stochastic atmospheric forcing leads to a large increase in the ensemble spread of forecast experiments performed using the 1994-1995 stochastic forcing (blue shading in Fig. 13). In this *1994-1995 Stochastic Ensemble*, the spread in the initial states and the variations in the stochastic atmospheric forcing across ensemble members is large enough such that some ensemble members end up with negative Niño

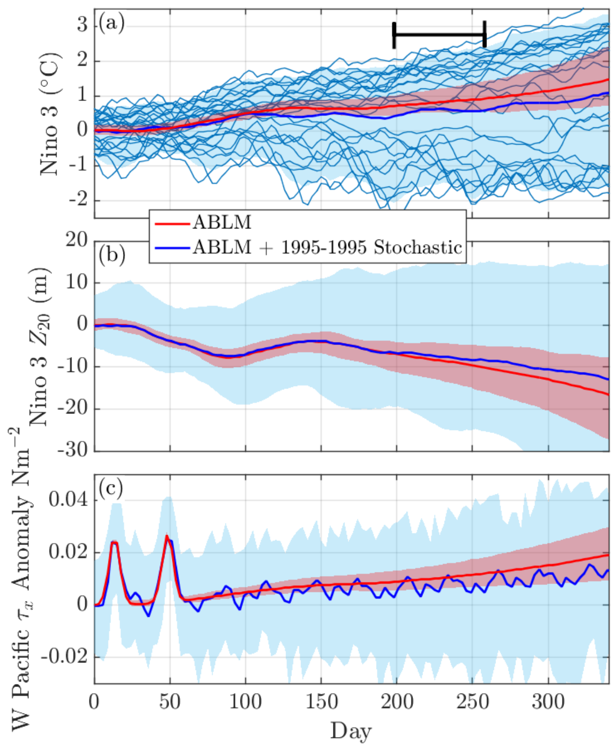

Fig. 13 As for Fig. 10 except comparing the results of two WWB coupled experiments (with coupling coefficient $R^F = 1.0$) with (blue) and without (black) additional 1994-1995 stochastic atmospheric forcing (see Section 2.6.2).

3 anomalies despite the two externally-imposed WWBs. Clearly, here the ensemble spread induced by the atmospheric forcing variability is larger than that coming from intrinsic oceanic processes. Again quantified $5-7$ months following the second WWB, the *1994-1995 Stochastic Ensemble* Niño 3 SST forecast spread is $\pm 1.91°$C compared to the $\pm 0.34°$C in the *ABLM Ensemble* (see Table 1). Therefore in this case oceanic intrinsic variability contributes around 18% of the ensemble spread. While this is much less than the 72% contribution found using the high-pass filter, it still suggests that intrinsic oceanic processes may make an appreciable contribution to the stochastic forcing of ENSO.

6 Summary and Conclusions

We have examined the impact of oceanic internal variability, associated with Tropical Instability Waves, on ENSO irregularity and predictability using a hybrid coupled model. We have focused on the July-December season when oceanic internal variability is seasonally largest and when ENSO events typically grow. By eliminating all sources of internal atmospheric variability (through the use of a simple atmospheric model) we have quantified the impact of oceanic internal variability on the growth rate and amplitude of coupled events subsequent to a given series of wind bursts in the western Pacific. In this idealized setup we find that oceanic internal variability can result in an ensemble spread of approximately $\pm 45\%$ of the size of the ensemble mean Niño 3 SST anomaly for an El Niño event (Table 1). For example, using a statistical coupling coefficient of 1.0 the Niño 3 SST anomaly six-months following the second of a series of two WWBs can range between 0.5°C to 1.2°C due to the initial state and evolution of the TIW field (Fig. 10).

We have also compared the variability coming from oceanic internal processes to atmospheric internal variability, typically thought to provide the stochastic forcing of the ENSO cycle. Using various estimates of this atmospheric internal variability, we found that oceanic intrinsic processes contribute between 18% and 72% of the ensemble spread in the idealized coupled forecasts (Table 1 and Figs. 12 and 13). The upper limit of 72% corresponds to when atmospheric internal variability is estimated by retaining only frequencies faster than two-months in the atmospheric forcing. As such a high-pass filter removes the low-frequency tail of the atmospheric noise, we expect that 72% is an overestimate of the potential influence of oceanic variability. The lower limit of 18% is obtained in contrast by removing all atmospheric forcing variability that is linearly associated with SST variability (using an SVD method; see Section 2.6). Therefore, this could potentially be an underestimate of the contribution of oceanic noise, as the forcing still includes atmospheric variability that is non-linearly related to SST variability.

The contribution of oceanic internal variability to ENSO irregularity reported here is derived from an idealized model setup and relies on a number of simplifying assumptions. Firstly, our simulations focus on the strong TIW season and do not contain a seasonal cycle in the mean circulation, known to be crucial for ENSO dynamics (Tziperman et al, 1997; Stein et al, 2014; Abellán and McGregor, 2015). Secondly, our ensemble simulations all start from initial neutral states without anomalous build-up or deficit of WWV. Such initial WWV anomalies are known to be important for the development of future events (Meinen and McPhaden, 2001; Fedorov et al, 2015) and, combined with seasonal variations, can impact the magnitude of the SST anomalies resulting from WWBs (Puy et al, 2016). Thirdly, our statistical atmosphere was simplified, using a single SVD mode that captures the first-order atmosphere-ocean coupling. The statistical coupling also depends on a coupling coefficient which is difficult to constrain, although we found that the impact of oceanic internal variability on the Niño 3 SST ensemble spread relative to the ensemble mean in the *ABLM Ensemble* was insensitive to this coefficient (Table 1). Despite these shortcomings, our model and experimental design serve to provide a first order estimate of the contribution of oceanic internal variability to ENSO growth and irregularity. More work is required to more precisely quantify this effect. However, such quantification remains difficult in more complex coupled systems as it requires a method to attribute portions of the observed coupled variability to either oceanic or atmospheric processes.

An additional factor that we have not examined in this study is the influence of TIWs on small-scale wind variability in the central and eastern Pacific (e.g. Chelton et al, 2001; Narapusetty and Kirtman, 2014; Zhang, 2014). These previous studies show that small-scale atmospheric variability can be driven directly by TIW SST anomalies, and may also impact on the irregularity and predictability of the coupled system (Jochum et al, 2007a).

Our results suggest that it is important to correctly represent small-scale non-linear oceanic processes in order to successfully capture all the processes that contribute to ENSO irregularity. A correct representation of small-scale oceanic processes requires an ocean model with resolution higher than the typical 1° used in many global coupled models (Graham, 2014). These models may therefore miss a potentially important component of the stochastic forcing of ENSO contributing to an under-representation of ENSO in these models (see e.g. Santoso et al, 2017). The under-representation of TIWs may also impact seasonal forecast ensembles that employ relatively low resolution ocean components (also see Ham and Kang, 2011). The contribution of TIWs to ENSO should thus be more carefully considered in future modeling studies and observations.

Acknowledgements This study benefited from discussions with Vishal Dixit and comments from two anonymous reviewers. A.S. and M.H.E. are supported by the Earth Science and Climate Change Hub of the Australian Government's National Environmental Science Programme (NESP) and the Centre for Southern Hemisphere Oceans Research (CSHOR), a joint research Centre for Southern Hemisphere Ocean Research between QNLM, CSIRO, UNSW and UTAS. The altimeter products were produced and distributed by the Copernicus Marine and Environment Monitoring Service (CMEMS) (`http://www.marine.copernicus.eu`). We thank the TAO Project Office of NOAA/PMEL for providing the TAO data. This research was undertaken with the assistance of resources and services from the National Computational Infrastructure (NCI), which is supported by the Australian Government.

Appendix: The Atmospheric Boundary Layer Model

As discussed in Section 2, we use an Atmospheric Boundary Layer Model (ABLM) to freely determine the air temperature T_{air} and air humidity q_{air}. Our implementation is based on the cheapAML model of Deremble et al (2013), following earlier work by Seager et al (1995). The model solves single layer advection-diffusion equations for T_{air} and q_{air},

$$\frac{\partial T_{air}}{\partial t} = -\nabla_h \cdot \left(\boldsymbol{U} T_{air} - \kappa \nabla_h T_{air}\right) + \frac{1}{\rho_a C_p h}\left(F^+ - F^-\right) - \frac{1}{r_T}\left(T_{air} - T_b\right), \tag{A.1}$$

$$\frac{\partial q_{air}}{\partial t} = -\nabla_h \cdot \left(\boldsymbol{U} q_{air} - \kappa \nabla_h q_{air}\right) + \frac{1}{h}\left(F_Q^+ - F_Q^-\right) - \frac{1}{r_T}\left(q_{air} - q_b\right), \tag{A.2}$$

where $\boldsymbol{U}$ is the prescribed 10m wind field, κ is an isotropic horizontal diffusivity, ρ_a is the density of air, C_p is the heat capacity of air, h is the spatially variable depth of the atmospheric boundary layer, r_T is a restoring time-scale that is non-zero only over land (where it takes the value 0.1 days) and T_b and q_b are background restoring fields for air temperature and humidity.

As discussed in Deremble et al (2013), the imbalance of heat loss from the top of the boundary layer, F^+, and heat gain from the ocean F^- are parameterized using long-wave radiative fluxes and the air-sea sensible heat flux (solar radiation and the latent heat flux both pass through the boundary layer at first order). Heat is lost via long-wave radiation from the top of the boundary layer using an average lapse rate of $0.0098°\mathrm{Cm}^{-1}$. The upper and lower fluxes of moisture, F_Q^+ and F_Q^- are represented by evaporation and entrainment at the top of the boundary layer. The advecting wind-velocities $\boldsymbol{U}$, the boundary and over-land air temperature and air humidity and the spatially variable boundary layer depth h are taken from the ERA Interim 1980-2014 July-December average discussed above. All air-sea fluxes are determined using the ROMS bulk flux routines, based on Fairall et al (1996). Due to the constant wind speeds and lack of storm systems, we use a large diffusivity of $\kappa = 5 \times 10^5 \mathrm{m}^2\mathrm{s}^{-1}$.

In regions with high SST, the air temperature determined by the ABLM has a tendency to warm too much due to the absence of convection. This excessive warming in convective regions was also noted by Deremble et al (2013), but they did not suggest a solution other than restoring. In order to avoid this unphysical warming we include a simple threshold on the surface air temperature, chosen as 28°C. This crudely models the effects of convection, which above this threshold mixes the air column vertically until the surface air temperature is once again below the threshold, returning the system to marginal stability. The presence of a threshold SST of around $27 - 28°\mathrm{C}$ above which convection occurs is well supported in the literature (e.g. Graham and Barnett, 1987; Johnson and Xie, 2010). Wind convergence also plays an important role in modulating convection (Graham and Barnett, 1987). However, as we have a temporally constant wind field and do not resolve any synoptic scale variability we do not include a parameterization for this effect.

Our implementation of the ABLM includes several tuning parameters, such as the effective height of upwards long-wave radiation out of the boundary layer, the convective air temperature threshold and the constant of proportionality α relating the entrainment of humidity at the top of the boundary layer to the surface fluxes. The best parameter set was found to be $\alpha = 0.3$ (compared to the value of 0.25 used by Deremble et al (2013)), a 28°C threshold and long-wave radiation from the top of the boundary layer. The remaining biases include a tendency to be too warm and wet in the warm and wet regions and too cool and dry in the cool regions (as also noted by Deremble et al (2013) in a fixed SST experiment). This bias is likely due to the absence of low-cloud feedbacks.

References

Abellán E, McGregor S (2015) The role of the southward wind shift in both, the seasonal synchronization and duration of ENSO events. Climate Dynamics pp 1–19, DOI 10.1007/s00382-015-2853-1

An S (2008) Interannual variations of the tropical ocean instability wave and ENSO. J Climate 21(15):3680–3686, DOI 10.1175/2008JCLI1701.1

An SI (2009) A review of interdecadal changes in the nonlinearity of the El Niño-Southern Oscillation. Theoretical and Applied Climatology 97(1):29–40, DOI 10.1007/s00704-008-0071-z

Arbic BK, Müller M, Richman JG, Shriver JF, Morten AJ, Scott RB, Sérazin G, Penduff T (2014) Geostrophic turbulence in the frequency-wavenumber domain: Eddy-driven low-frequency variability. J Phys Oceanogr 44(8):2050–2069, DOI 10.1175/JPO-D-13-054.1

Balmaseda MA, Mogensen K, Weaver AT (2013) Evaluation of the ECMWF ocean reanalysis system ORAS4. Q J Roy Meteorol Soc 139(674):1132–1161, DOI 10.1002/qj.2063

Blanke B, Neelin JD, Gutzler D (1997) Estimating the effect of stochastic wind stress forcing on ENSO irregularity. J Climate 10(7):1473–1486, DOI 10.1175/1520-0442(1997)010⟨1473:ETEOSW⟩2.0.CO;2

Chelton DB, Esbensen SK, Schlax MG, Thum N, Freilich MH, Wentz FJ, Gentemann CL, McPhaden MJ, Schopf PS (2001) Observations of coupling between surface wind stress and sea surface temperature in the eastern tropical Pacific. Journal of Climate 14(7):1479–1498, DOI 10.1175/1520-0442(2001)014⟨1479:OOCBSW⟩2.0.CO;2

Chiodi AM, Harrison DE, Vecchi GA (2014) Subseasonal atmospheric variability and El Niño waveguide warming: Observed effects of the Madden–Julian oscillation and westerly wind events. J Climate 27(10):3619–3642, DOI 10.1175/JCLI-D-13-00547.1

Contreras RF (2002) Long-term observations of tropical instability waves. J Phys Oceanogr 32(9):2715–2722

Cox MD (1980) Generation and propagation of 30-day waves in a numerical model of the Pacific. J Phys Oceanogr 10(8):1168–1186, DOI 10.1175/1520-0485(1980)010⟨1168:GAPODW⟩2.0.CO;2

Dee DP, Uppala SM, Simmons AJ, Berrisford P, Poli P, Kobayashi S, Andrae U, Balmaseda MA, Balsamo G, Bauer P, Bechtold P, Beljaars ACM, van de Berg L, Bidlot J, Bormann N, Delsol C, Dragani R, Fuentes M, Geer AJ, Haimberger L, Healy SB, Hersbach H, Hólm EV, Isaksen L, Kållberg P, Köhler M, Matricardi M, McNally AP, Monge-Sanz BM, Morcrette JJ, Park BK, Peubey C, de Rosnay P, Tavolato C, Thépaut JN, Vitart F (2011) The ERA-Interim reanalysis: Configuration and performance of the data assimilation system. Q J Roy Meteorol Soc 137(656):553–597, DOI 10.1002/qj.828

Deremble B, Wienders N, Dewar WK (2013) CheapAML: A simple, atmospheric boundary layer model for use in ocean-only model calculations. Mon Wea Rev 141(2):809–821, DOI 10.1175/MWR-D-11-00254.1

Dommenget D (2010) The slab ocean El Niño. Geophys Res Lett 37(20):L20,701, DOI 10.1029/2010GL044888

Dueing W, Hisard P, Katz E, Meincke J, Miller L, Moroshkin KV, Philander G, Ribnikov AA, Voigt K, Weisberg R (1975) Meanders and long waves in the equatorial atlantic. Nature 257:280–284, DOI 10.1038/257280a0

Eisenman I, Yu L, Tziperman E (2005) Westerly wind bursts: ENSO's tail rather than the dog? J Climate 18(24):5224–5238, DOI 10.1175/JCLI3588.1

Fairall CW, Bradley EF, Rogers DP, Edson JB, Young GS (1996) Bulk parameterization of air-sea fluxes for tropical ocean-global atmosphere coupled-ocean atmosphere response experiment. J Geophys Res 101(C2):3747–3764, DOI 10.1029/95JC03205

Fedorov AV, Hu S, Lengaigne M, Guilyardi E (2015) The impact of westerly wind bursts and ocean initial state on the development, and diversity of El Niño events. Climate Dynamics 44(5):1381–1401, DOI 10.1007/s00382-014-2126-4

Flament P, Kennan S, Knox R, Niiler P, Bernstein R (1996) The three-dimensional structure of an upper ocean vortex in the tropical Pacific ocean. Nature 383(6601):610–613, DOI 10.1038/383610a0

Frauen C, Dommenget D (2010) El Niño and La Niña amplitude asymmetry caused by atmospheric feedbacks. Geophys Res Lett 37(18):L18,801, DOI 10.1029/2010GL044444

Gebbie G, Eisenman I, Wittenberg A, Tziperman E (2007) Modulation of westerly wind bursts by sea surface temperature: A semistochastic feedback for ENSO. J Atmos Sci 64(9):3281–3295, DOI 10.1175/JAS4029.1

Graham NE, Barnett TP (1987) Sea surface temperature, surface wind divergence, and convection over tropical oceans. Science 238(4827):657–659, DOI 10.1126/science.238.4827.657

Graham T (2014) The importance of eddy permitting model resolution for simulation of the heat budget of tropical instability waves. Ocean Model 79(0):21 – 32, DOI 10.1016/j.ocemod.2014.04.005

Ham YG, Kang IS (2011) Improvement of seasonal forecasts with inclusion of tropical instability waves on initial conditions. Climate Dynamics 36(7-8):1277–1290, DOI 10.1007/s00382-010-0743-0

Hayashi M, Watanabe M (2017) ENSO complexity induced by state dependence of westerly wind events. J. Climate 30(9):3401–3420, DOI 10.1175/JCLI-D-16-0406.1

Holmes RM, Thomas LN (2016) Modulation of tropical instability wave intensity by equatorial Kelvin waves. J Phys Oceanogr 46:2623–2643, DOI 10.1175/JPO-D-16-0064.1

Hu S, Fedorov AV, Lengaigne M, Guilyardi E (2014) The impact of westerly wind bursts on the diversity and predictability of El Niño events: An ocean energetics perspective. Geophys Res Lett 41(13):2014GL059,573, DOI 10.1002/2014GL059573

Imada Y, Kimoto M (2012) Parameterization of tropical instability waves and examination of their impact on ENSO characteristics. J Climate 25(13):4568–4581, DOI 10.1175/JCLI-D-11-00233.1

Jochum M, Murtugudde R (2004) Internal variability of the tropical Pacific ocean. Geophys Res Lett 31(14), DOI 10.1029/2004GL020488

Jochum M, Murtugudde R (2005) Internal variability of Indian ocean SST. J Climate 18(18):3726–3738, DOI 10.1175/JCLI3488.1

Jochum M, Murtugudde R (2006) Temperature advection by tropical instability waves. J Phys Oceanogr 36(4):592–605, DOI 10.1175/JPO2870.1

Jochum M, Cronin M, Kessler W, Shea D (2007a) Observed horizontal temperature advection by tropical instability waves. Geophys Res Lett 34(9), DOI 10.1029/2007GL029416

Jochum M, Deser C, Phillips A (2007b) Tropical atmospheric variability forced by oceanic internal variability. J Climate 20(4):765–771, DOI 10.1175/JCLI4044.1

Jochum M, Danabasoglu G, Holland M, Kwon YO, Large WG (2008) Ocean viscosity and climate. J Geophys Res 113(C6):C06017, DOI 10.1029/2007JC004515,

Johnson NC, Xie SP (2010) Changes in the sea surface temperature threshold for tropical convection. Nature Geosci 3(12):842–845, DOI 10.1038/ngeo1008

Keen RA (1982) The role of cross-equatorial tropical cyclone pairs in the Southern Oscillation. Mon Wea Rev 110(10):1405–1416, DOI 10.1175/1520-0493(1982)110⟨1405:TROCET⟩2.0.CO;2

Kirtman BP (1997) Oceanic rossby wave dynamics and the ENSO period in a coupled model. J Climate 10(7):1690–1704, DOI 10.1175/1520-0442(1997)010⟨1690:ORWDAT⟩2.0.CO;2

Large W, Yeager S (2004) Diurnal to decadal global forcing for ocean and sea-ice models: the data sets and flux climatologies. National Center for Atmospheric Research

Large WG, McWilliams JC, Doney SC (1994) Oceanic vertical mixing: A review and a model with a nonlocal boundary layer parameterization. Rev Geophys 32(4):363–403, DOI 10.1029/94RG01872

Latif M, Sperber K, Arblaster J, Braconnot P, Chen D, Colman A, Cubasch U, Cooper C, Delecluse P, Dewitt D, Fairhead L, Flato G, Hogan T, Ji M, Kimoto M, Kitoh A, Knutson T, Le Treut H, Li T, Manabe S, Marti O, Mechoso C, Meehl G, Power S, Roeckner E, Sirven J, Terray L, Vintzileos A, Voß R, Wang B, Washington W, Yoshikawa I, Yu J, Zebiak S (2001) ENSIP: the El Niño simulation intercomparison project. Climate Dynamics 18(3):255–276, DOI 10.1007/s003820100174

Legeckis R (1977) Long waves in the eastern equatorial Pacific ocean: A view from a geostationary satellite. Science 197(4309):1179–1181

Levine A, Jin F, McPhaden M (2016) Extreme noise-extreme El Niño: How state-dependent noise forcing creates El Niño-la Niña asymmetry. J Climate DOI 10.1175/JCLI-D-16-0091.1

Levine AFZ, Jin FF (2017) A simple approach to quantifying the noise–ENSO interaction. Part I: deducing the state-dependency of the windstress forcing using monthly mean data. Climate Dynamics 48(1):1–18, DOI 10.1007/s00382-015-2748-1

Locarnini RA, Mishonov AV, Antonov JI, Boyer TP, Garcia HE, Baranova OK, Zweng MM, Paver CR, Reagan JR, Johnson DR, Hamilton M, Seidov D (2013) World Ocean Atlas 2013, Volume 1: Temperature. NOAA Atlas

NESDIS 73:40, S. Levitus, Ed., A. Mishonov Technical Ed.

Lyman J, Johnson G, Kessler W (2007) Distinct 17- and 33-day tropical instability waves in subsurface observations. J Phys Oceanogr 37(4):855–872, DOI 10.1175/JPO3023.1

Marchesiello P, Capet X, Menkes C, Kennan S (2011) Submesoscale dynamics in tropical instability waves. Ocean Model 39(1-2):31–46, DOI 10.1016/j.ocemod.2011.04.011

Masina S, Philander S, Bush A (1999) An analysis of tropical instability waves in a numerical model of the Pacific ocean 2. Generation and energetics of the waves. J Geophys Res 104(29):637–29, DOI 10.1029/1999JC900226

McGregor S, Ramesh N, Spence P, England MH, McPhaden MJ, Santoso A (2013) Meridional movement of wind anomalies during ENSO events and their role in event termination. Geophys Res Lett DOI 10.1002/grl.50136

Meinen CS, McPhaden MJ (2001) Interannual variability in warm water volume transports in the equatorial pacific during 1993-1999. J Phys Oceanogr 31(5):1324–1345, DOI 10.1175/1520-0485(2001)031⟨1324:IVIWWV⟩2.0.CO;2

Menkes C, Vialard J, Kennan S, Boulanger J, Madec G (2006) A modeling study of the impact of tropical instability waves on the heat budget of the eastern equatorial Pacific. J Phys Oceanogr 36(5):847–865, DOI 10.1175/JPO2904.1

Moore AM, Kleeman R (1999) Stochastic forcing of ENSO by the intraseasonal oscillation. J Climate 12(5):1199–1220, DOI 10.1175/1520-0442(1999)012⟨1199:SFOEBT⟩2.0.CO;2

Narapusetty B, Kirtman B (2014) Sensitivity of near-surface atmospheric circulation to tropical instability waves. Climate Dynamics 42(11-12):3139–3150, DOI 10.1007/s00382-014-2167-8

Neelin JD (1990) A hybrid coupled general circulation model for El Niño studies. J Atmos Sci 47(5):674–693, DOI 10.1175/1520-0469(1990)047⟨0674:AHCGCM⟩2.0.CO;2

Penduff T, Juza M, Barnier B, Zika J, Dewar WK, Treguier AM, Molines JM, Audiffren N (2011) Sea level expression of intrinsic and forced ocean variabilities at interannual time scales. J Climate 24(21):5652–5670, DOI 10.1175/JCLI-D-11-00077.1

Pezzi LP, Vialard J, Richards KJ, Menkes C, Anderson D (2004) Influence of ocean-atmosphere coupling on the properties of tropical instability waves. Geophys Res Lett 31(16), DOI 10.1029/2004GL019995

Philander S (1976) Instabilities of zonal equatorial currents. J Geophys Res 81(21):3725–3735, DOI 10.1029/JC081i021p03725

Puy M, Vialard J, Lengaigne M, Guilyardi E, Voldoire A, Madec G (2016) Modulation of equatorial pacific sea surface temperature response to westerly wind events by the oceanic background state. Climate Dynamics pp 1–25, DOI 10.1007/s00382-016-3480-1

Santoso A, McPhaden MJ, Cai W (2017) The defining characteristics of ENSO extremes and the strong 2015/2016 El Niño. Reviews of Geophysics 55(4):1079–1129, DOI 10.1002/2017RG000560

von Schuckmann K, Brandt P, Eden C (2008) Generation of tropical instability waves in the Atlantic Ocean. J Geophys Res 113(C8):C08,034, DOI 10.1029/2007JC004712

Seager R, Blumenthal MB, Kushnir Y (1995) An advective atmospheric mixed layer model for ocean modeling purposes: Global simulation of surface heat fluxes. J Climate 8(8):1951–1964, DOI 10.1175/1520-0442(1995)008⟨1951:AAAMLM⟩2.0.CO;2

Shchepetkin A, McWilliams J (2005) The Regional Oceanic Modeling System (ROMS): A split-explicit, free-surface, topography-following-coordinate oceanic model. Ocean Model 9(4):347–404, DOI 10.1016/j.ocemod.2004.08.002

Small RJ, Richards KJ, Xie SP, Dutrieux P, Miyama T (2009) Damping of tropical instability waves caused by the action of surface currents on stress. J Geophys Res 114(C4), DOI 10.1029/2008JC005147

Small RJ, Curchitser E, Hedstrom K, Kauffman B, Large WG (2015) The Benguela upwelling system: Quantifying the sensitivity to resolution and coastal wind representation in a global climate model. J Climate 28(23):9409–9432, DOI 10.1175/JCLI-D-15-0192.1

Stein K, Timmermann A, Schneider N, Jin FF, Stuecker MF (2014) ENSO seasonal synchronization theory. J Climate 27(14):5285–5310, DOI 10.1175/JCLI-D-13-00525.1

Syu HH, Neelin JD, Gutzler D (1995) Seasonal and interannual variability in a hybrid coupled GCM. J Climate 8(9):2121–2143, DOI 10.1175/1520-0442(1995)008⟨2121:SAIVIA⟩2.0.CO;2

Tziperman E, Zebiak SE, Cane MA (1997) Mechanisms of seasonal-ENSO interaction. J Atmos Sci 54(1):61–71, DOI 10.1175/1520-0469(1997)054⟨0061:MOSEI⟩2.0.CO;2

Willett CS, Leben RR, Lavín MF (2006) Eddies and tropical instability waves in the eastern tropical Pacific: A review. Prog Oceanogr 69:218 – 238, DOI 10.1016/j.pocean.2006.03.010

Zavala-Garay J, Moore A, Perez C, Kleeman R (2003) The response of a coupled model of ENSO to observed estimates of stochastic forcing. J Climate 16(17):2827–2842, DOI 10.1175/1520-0442(2003)016⟨2827:TROACM⟩2.0.CO;2

Zelle H, Appeldoorn G, Burgers G, van Oldenborgh GJ (2004) The relationship between sea surface temperature and thermocline depth in the eastern equatorial pacific. J Phys Oceanogr 34(3):643–655, DOI 10.1175/2523.1

Zhang C (2005) Madden-Julian Oscillation. Reviews of Geophysics 43(2):RG2003, DOI 10.1029/2004RG000158

Zhang RH (2014) Effects of tropical instability wave (TIW)-induced surface wind feedback in the tropical pacific ocean. Climate Dynamics 42(1):467–485, DOI 10.1007/s00382-013-1878-6

Zhang RH (2015) A hybrid coupled model for the Pacific ocean-atmosphere system. Part I: Description and basic performance. Advances in Atmospheric Sciences 32(3):301–318, DOI 10.1007/s00376-014-3266-5

Zhang RH (2016) A modulating effect of Tropical Instability Wave (TIW)-induced surface wind feedback in a hybrid coupled model of the tropical Pacific. J Geophys Res 121, DOI 10.1002/2015JC011567

Zhang RH, Busalacchi AJ (2008) Rectified effects of tropical instability wave (TIW)-induced atmospheric wind feedback in the tropical Pacific. Geophys Res Lett 35(5), DOI 10.1029/2007GL033028

Zweng M, Reagan J, Antonov J, Locarnini R, Mishonov A, Boyer T, Garcia H, Baranova O, Johnson D, DSeidov, Biddle M (2013) World Ocean Atlas 2013, Volume 2: Salinity. NOAA Atlas NESDIS 74:39, S. Levitus, Ed., A. Mishonov Technical Ed.